NTIA Report 99-366

Spectrum Measurements for an RF-Driven Lighting Device

Roger A. Dalke
Patricia J. Raush
Frank H. Sanders
Jeanne M. Ratzloff

U.S. DEPARTMENT OF COMMERCE
William M. Daley, Secretary

Larry Irving, Assistant Secretary
for Communications and Information

May 1999

This Page Intentionally Left Blank

This Page Intentionally Left Blank

PRODUCT DISCLAIMER

Certain commercial companies, equipment, instruments, and materials are identified in this report to specify adequately the technical aspects of the reported results. In no case does such identification imply recommendation or endorsement by the National Telecommunications and Information Administration, nor does it imply that the material or equipment identified is necessarily the best available for the purpose.

ACKNOWLEDGMENTS

The Institute for Telecommunication Sciences (ITS) would like to acknowledge G. Koepke and the Fields and Interference Meteorology Group of the National Institute of Standards and Technology for their contribution to this work. Their group provided the transverse electromagnetic (TEM) cell and technical support required to obtain the TEM cell measurements. ITS appreciates their support towards this measurement effort.

CONTENTS

This Page Intentionally Left Blank

This Page Intentionally Left Blank

SPECTRUM MEASUREMENTS FOR AN RF-DRIVEN LIGHTING DEVICE

Roger A. Dalke, Patricia J. Raush, Frank H. Sanders and Jeanne M. Ratzloff[1]

New lighting devices that emit radio frequencies are being developed for commercial use. Since such devices may interfere with communication systems that utilize the radio spectrum, it is essential that the emission characteristics be carefully analyzed. This report describes the spectral emission characteristics of a radio frequency (nominally 2.5 MHz) driven lighting device that is under development for commercial use in the U.S. A combination of near field measurement techniques and a theoretical model were used to determine emitted field levels. This report presents the results of the measurements and details measurement and analysis methods used to determine the emissions spectrum. The results presented include the theoretical model of the radio frequency source that can be used to predict spectral emissions of arrays of such lighting devices.

Key words: Compact Radio Spectrum Measurement System (CRSMS); Data Acquisition (DA); RF lighting device; spectral emissions; RF interference

1. INTRODUCTION

The Institute for Telecommunication Sciences (ITS) in cooperation with the General Electric Company (GE) studied the emission characteristics of a radio frequency (RF)-driven lighting device. Devices that generate RF emissions, such as the new lighting device, have the potential to substantially impact other devices that currently use the radio spectrum. One way to assess the possible impact on the spectrum is to measure the emissions from individual units. This report describes a study conducted by ITS to determine spectral emissions of the RF-driven lighting device.

A particular challenge to measuring RF emissions from an unknown source is the selection of an environment where the interactions of the device under test and the environment are well understood. At the frequencies at which the lighting device operates (one to several megahertz), the wavelength of the fundamental radiation will exceed 100 m. This is substantially larger than the typical dimensions of the space in which the device might operate. The resulting electromagnetic interactions in such environments, particularly radiation patterns, may be difficult to analyze, even though the measurements themselves may not be difficult to perform. In this study, measurements were conducted on an outdoor antenna test range and in a transverse electromagnetic (TEM) cell. The advantage of these two particular environments is that their electromagnetic interactions are simplified and reasonably well understood; this allows for an accurate characterization of the RF

[1]The authors are with the Institute for Telecommunication Sciences, National Telecommunications and Information Administration, U.S. Department of Commerce, Boulder, CO 80303-3328

source. Once the source is properly characterized, models can be developed that will allow the prediction of emissions in more complex environments (e.g., arrays of such devices in buildings). The results presented in this report also include indoor measurements. These indoor measurements were used to determine the conducted current levels, emissions as a function of input voltage, and time domain envelope scans.

The measurements described in this report are primarily designed to: (1) determine the RF emission spectrum (fundamental and harmonics) in the environments described above and (2) characterize the RF source in terms of simple analytical models. Both outdoor and indoor measurements were performed using a compact radio spectrum measurement system (CRSMS) developed by ITS. A description of the measurement equipment is provided in Section 2.1 of this report. TEM cell measurements were performed at the National Institute of Standards and Technology (NIST) using the measurement system and software developed by NIST [1, 2]. The measurement analysis includes the calculation of field levels in the near field of the device, equivalent dipole moments developed from TEM cell measurements, and a comparison of measured field levels with a numerical model of the device developed for this study. Important results, e.g. radiated power, are presented in Section 4 of the report. The large number of spectrum analyzer scans supporting this analysis are presented in the Appendix.

This investigation entails determining the RF emissions at distances relatively close to the device. Therefore, it was necessary to insure that the equipment and methods did not modify the radiation field of the device. A simple dipole probe field strength measurement was deemed inadequate for this purpose. To obtain reliable results, a measurement system using four probing techniques was devised as described in Section 2. In addition, a simulation model, based on the general geometric structure of the device, was developed. This model was used to predict the radiation pattern and its magnitude. The model data was in agreement with the pattern obtained using the four probes. The mathematical development of the model and the equations for calculating the electromagnetic fields are presented in this report.

2. MEASUREMENT SYSTEM

The system used to measure the RF emissions from the lighting device is the CRSMS. This compact system is used by ITS in support of measurement tasks for the National Telecommunications and Information Administration (NTIA) and other agencies. This system is portable and usually available on short notice. It can be either flown or driven to measurement locations, and has highly flexible deployment modes. If necessary, this compact measurement system may be operated in a mobile configuration. For this particular application, the measurement system was used at various locations: on an antenna range, in a shielded room, and in a laboratory environment.

2.1 Hardware: Compact Radio Spectrum Measurement System

The primary components of the CRSMS used in these measurements were a spectrum analyzer, a personal computer (PC), and appropriate antennas and probes. The system block diagram is shown in Figure 1. A CRSMS configuration often includes dynamic RF attenuation, tracking preselection, and preamplification. However, initial measurements on the GE lighting device demonstrated that these options were not required for this study.

The spectrum analyzer used for the measurements presented in this report was a Hewlett Packard (HP) 8566B. An RF line having minimal loss connected the spectrum analyzer to the various measurement antennas. At the frequencies measured, the spectrum analyzer noise figure was 25 dB. Manufacturer-recommended pre-calibration of the analyzer was relied upon to provide absolute amplitude accuracy of ±2 dB in the measurements. Four different antennas were used: an Antenna Research Associates, Inc., (ARA) 12-in passive loop, two Electro-Mechanics Company (EMCO) probes, and a Pearson Electronics current monitor (see Section 2.3). Additional data were acquired using a TEM cell.

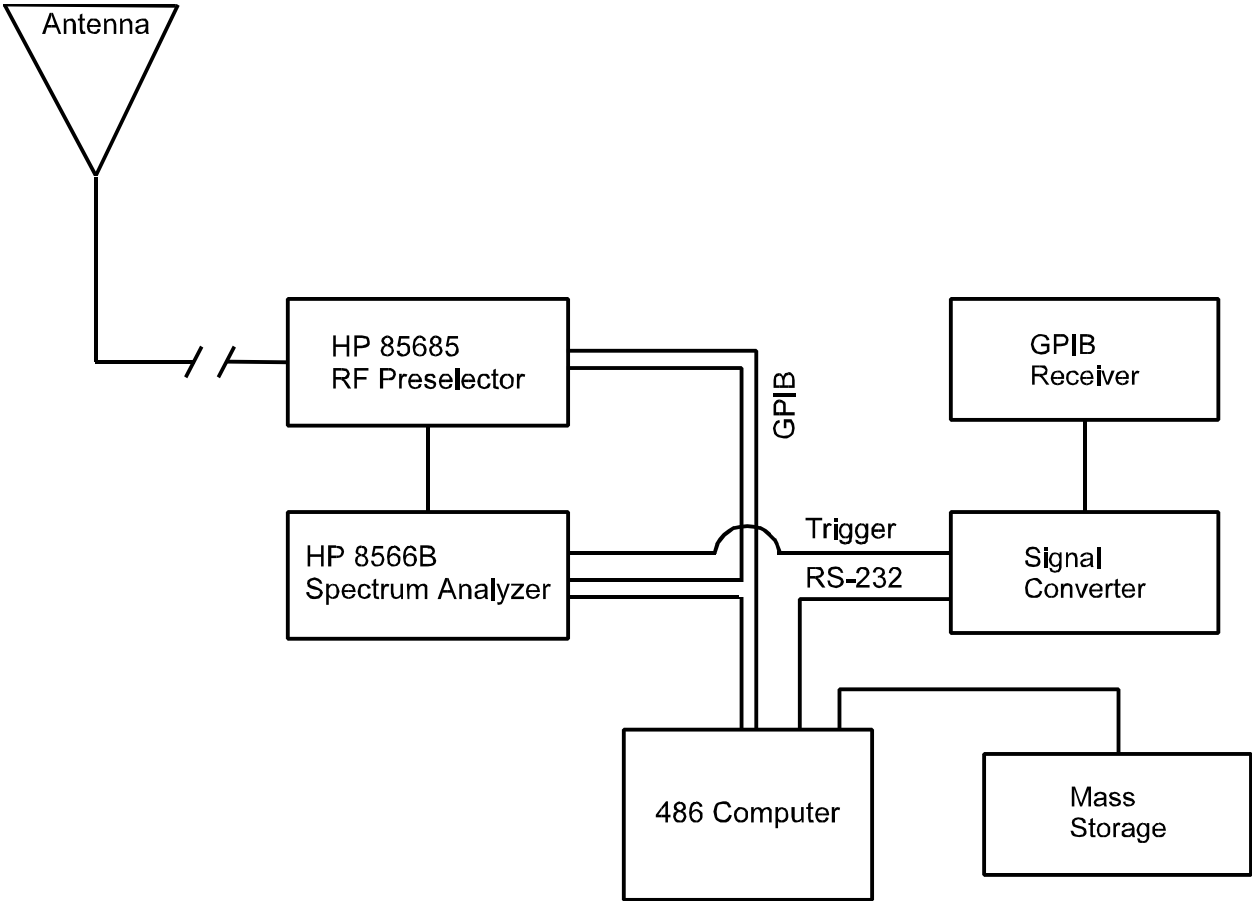

Figure 1. System block diagram of the CRSMS.

2.2 Software: Data Acquisition

The computer was configured with Data Acquisition (DA) software that was developed at ITS specifically for general-purpose spectrum measurements. For these measurements, we used the DA software to select the desired frequency or range of frequencies and to make the required spectrum (power versus frequency) and time (power versus time) scans. The resulting measurement scans show received power in the measurement bandwidth (usually 1 kHz), at the antenna terminals (50 ohms) and in decibels relative to a mW (dBm).

The DA software is an MS DOS-based software package that integrates commercial measurement instruments into a powerful RF signal acquisition and analysis solution tool. DA runs on any 80386 (or higher) IBM-compatible computer with a National Instruments GPIB interface card. The software makes use of GPIB bus interfaces on measurement instruments to command the instrument settings, coordinate signal acquisition, and retrieve data. The software currently can control 17 common instruments, including spectrum analyzers, digital oscilloscopes, pulse analyzers, RF preselectors, and antenna control systems, as well as custom instruments. The resulting data is stored in an IBM compatible format which can be viewed and analyzed on any PC running DA.

General measurement parameters were set within the software. Typically, we used resolution and video bandwidths of 1 kHz, a frequency span of 20 kHz, and a sweep time of 300 ms. The measurement bandwidths were selected to be as narrow as possible (so as to show maximum resolution on the signals of interest) while still being wide enough to convolve virtually all of the power in the spectral emissions (thus providing maximal signal-to-noise ratio for the measurement). The measurement reference level (related to spectrum analyzer IF gain) and RF attenuation settings in the analyzer were adjusted on a scan-by-scan basis. This put the entire amplitude range of the spectral emissions from the device within the dynamic range of the analyzer on each measurement scan.

The spectrum and time data collected by the CRSMS were retrieved by the computer and displayed on the computer monitor. All raw data were saved and recorded on magnetic media. Copies of these are available upon request. The magnetically-stored data may be retrieved by the DA program and its appropriate support files. Copies of DA.exe and its support files are also available.

The results presented in this report are based on a considerable amount of the raw data. The results presented here should suffice to show all pertinent results for each measurement.

2.3 Antennas and Probes

Field measurements were performed using an Antenna Research Associates, Inc., (ARA) 12-in passive loop, two EMCO probes (6-cm loop and e-field ball) and a Pearson Electronics current monitor. Calibration charts are included for the 12-in passive loop and the two EMCO probes (see Figures 2, 3, and 4, respectively). Because the lighting device was determined to behave primarily as a magnetic dipole source, the 6-cm loop was determined to provide the most efficient coupling to the device's RF emissions. Thus, the EMCO 6-cm loop was used for most of the measurements

presented in this report. Note that to obtain the magnetic field, the free space plane wave impedance had to be subtracted from the 6-cm loop performance factor.

The Pearson Electronics, Inc., Wide Band Current Monitor/Pulse Current Monitor (Model 110) with an output in 0.1 volts/amp was used for the current measurement performed in a shielded room.

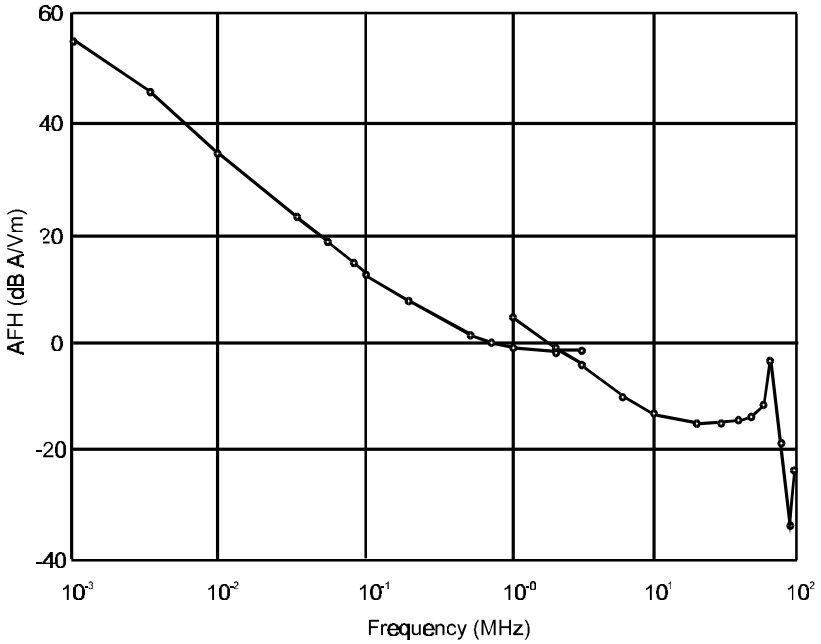

Figure 2. Calibration curve for the 12-in passive loop (PLA-130/A Serial #1005) provided and used with written permission of Antenna Research Associates, Inc., 10/19/94.

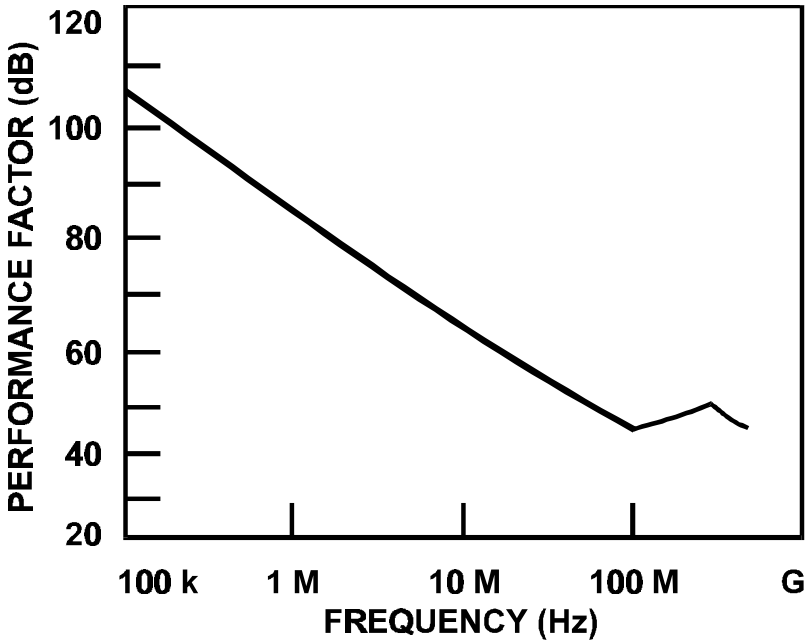

Figure 3. Performance factor for the EMCO 6-cm loop (Model #901) probe.

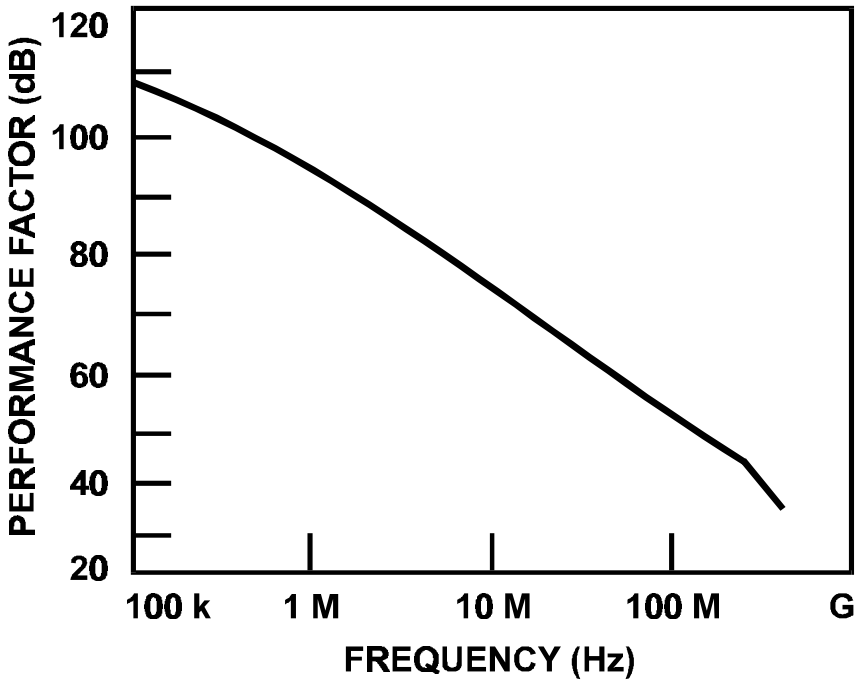

Figure 4. Performance factor for the EMCO e-field ball probe (Model #904).

Figures 3 and 4 are taken from the EMCO Model 7405 Near-Field Probe Set User's Manual and used with written permission of The Electro-Mechanics Company, 09/14/98.

3. SIMULATION MODEL

A simulation model of the device under test was developed for comparison with measurements. This model uses a finite difference time domain (FDTD) solution to Maxwell's curl equations. The development of time domain finite difference equations for the solution of electromagnetic boundary value problems has been the subject of numerous publications (see for example [3, 4, 5]). In some sense, each implementation is unique in that techniques that provide a reasonable approximation for the problem at hand must be devised. For example, methods that implement sources and boundary conditions that do not adversely affect the result must be developed and tested. For this device, a normalized magnetic current source was used to provide the forcing function for the numerical solution to the partial differential equations. Metallic conductors were included at appropriate geometrical positions by setting the tangential components of the electric fields to zero (Figure 5). The general mathematical development of the simulation model is described below.

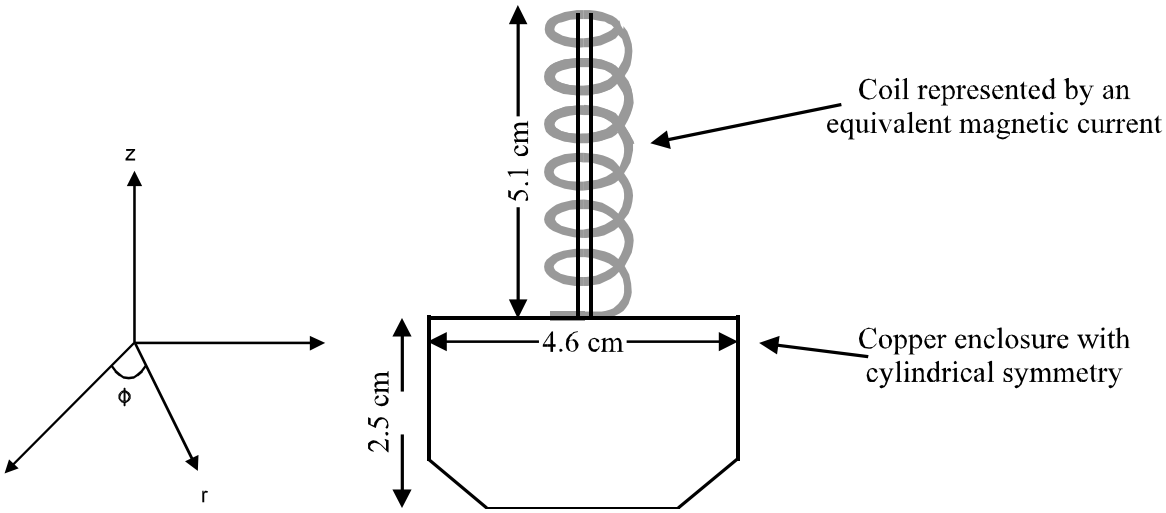

Figure 5. Cross-section of the light bulb conductors.

The RF emissions are completely described by Maxwell's equations. Using standard cylindrical coordinates (r, ϕ, z) and assuming azimuthal symmetry, Maxwell's curl equations are

$$\begin{aligned} \varepsilon \frac{\partial E_\phi}{\partial t} &= \frac{\partial H_r}{\partial r} - \frac{\partial H_z}{\partial z} \\ \mu \frac{\partial H_r}{\partial t} &= \frac{E_\phi}{\partial z} \\ \mu \frac{\partial H_z}{\partial t} &= -\frac{1}{r}\frac{\partial}{\partial r}(r E_\phi) - J_z^* \end{aligned} \qquad \textbf{(1)}$$

where the magnetic field has two components H_z and H_r; and the electric field has one component E_ϕ. For this model, a forcing function in the form of a *fictitious* magnetic current density J_z^* was used to represent a magnetic dipole source as described below. To construct the model, the equations are approximated by using central differencing of the field components of Equation 1 in both space and time, for example:

$$\frac{\partial E_\phi(t,r,z)}{\partial t} \approx \frac{E_\phi(t+\frac{\Delta t}{2},r,z) - E_\phi(t-\frac{\Delta t}{2},r,z)}{\Delta t}. \qquad \textbf{(2)}$$

The numerical algorithm is implemented by replacing the spatial and temporal coordinates by indices that represent physical space cylindrical coordinates. The resulting finite difference equations that define the model are:

$$
\begin{aligned}
E_\phi(i,j,n) &= E_\phi((i-1)\Delta r,(j-\frac{1}{2})\Delta z,(n-1)\Delta t)\\
H_r(i,j,n) &= H_r((i-1)\Delta r,(j-\frac{1}{2})\Delta z,(n-\frac{1}{2})\Delta t)\\
H_z(i,j,n) &= H_z((i-1)\Delta r,(j-\frac{1}{2})\Delta z,(n-\frac{1}{2})\Delta t)\\
E_\phi(i,j) &= E_\phi(i,j)+\frac{\Delta t}{\varepsilon}\left[\frac{H_r(i,j+1)-H_r(i,j)}{\Delta z}-\frac{H_z(i+1,j)-H_z(i,j)}{\Delta r}\right]\\
H_r(i,j) &= H_r(i,j)+\frac{\Delta t}{\mu}\frac{(E_\phi(i,j)-E_\phi(i,j-1))}{\Delta r}\\
H_z(i,j) &= H_z(i,j)-\frac{\Delta t}{\mu}\left[\frac{2}{(r_1+r_2)}\frac{(r_2E_\phi(i,j)-r_1E_\phi(i-1,j))}{\Delta r}-J_z^*(i,j)\right]\\
r_1 &= (i-\frac{3}{2})\Delta r\\
r_2 &= (i-\frac{1}{2})\Delta r.
\end{aligned}
\qquad \textbf{(3)}
$$

A difficulty occurs in the calculation of H_z due to singular behavior at the origin. This is overcome by applying Stoke's Theorem to Faraday's law which gives

$$\mu\frac{\partial}{\partial t}\int_S \vec{H}\cdot d\vec{A}=\oint\vec{E}\cdot d\vec{l}-\int_S \vec{J}^*\cdot d\vec{A}. \qquad \textbf{(4)}$$

Integrating the z component over a finite difference cell gives

$$\mu\frac{\partial H_z}{\partial t}=4\frac{E_\phi}{\Delta r}-J_z^*, \qquad \textbf{(5)}$$

and application of central differences yields the appropriate expression for calculating H_z at the origin

$$H_z(1,j) = H_z(1,j) - \frac{\Delta t}{\mu}\left[4\frac{E_\phi(1,j)}{\Delta r} - J_z^*(1,j)\right]. \quad \textbf{(6)}$$

The light bulb RF source for this application is a coil that was modeled by injecting a magnetic current (J_z^*) at the origin of the finite difference model. The relationship between J_z^* and the magnetic moment $\vec{m}$ of the RF coil can be determined using the definition of the magnetic dipole moment and the continuity equation for magnetic charges ρ^* and currents $\vec{J}^*$

$$\frac{\partial \vec{m}}{\partial t} = \int_V \vec{r}\,\rho^*\,dV = \int_V \vec{r}\,(\nabla\cdot\vec{J}^*)\,dV. \quad \textbf{(7)}$$

Application of the Divergence Theorem to Equation 7 gives the desired expression for the components of the magnetic moment. In this case only the *z* component is important, hence

$$\frac{\partial m_z}{\partial t} = \int_S z\vec{J}^*\cdot d\vec{A} - \int_V \nabla z\cdot\vec{J}^*\,dV. \quad \textbf{(8)}$$

The integrals were evaluated in terms of the finite difference model where the magnetic current density is constant within a cylinder centered at the origin that represented the RF coil (radius $\Delta r/2$ and height $N\Delta z$); hence,

$$\frac{\partial m_z}{\partial t} = \frac{\pi\,\Delta z(\Delta r)^2}{4}\sum_{j=1}^{N} J_z^*(j) = \pi\left(\frac{\Delta r}{2}\right)^2 N\Delta z\,J_z^*. \quad \textbf{(9)}$$

With this expression, the magnetic current forcing function in Equation 6 can be adjusted so that it properly characterizes the magnetic moment of the light bulb RF coil. This relationship can also be used to deduce the effective magnetic moment of an RF source by comparing measured and simulated results. Such a calculation is given in the following section.

The other important consideration in the solution of this problem is the implementation of proper boundary conditions. The desired solution is for a narrow band of frequencies which would require that a time domain simulation be run for a sufficient length of time that boundary interactions become important. As this is a near field problem, the implementation of typical radiating boundary conditions

is likely to have a significant negative impact on the solution. The approach used for this model is to drive the simulation with a narrow pulse so that the solution can be truncated prior to the arrival of the signal from the boundaries. The result is transformed to the frequency domain and the Green's function in terms of the fields as a function of magnetic moment is calculated. This approach requires the use of a pulse that has continuous high order derivatives at zero time to reduce numerical noise. In addition, the corresponding magnetic moment must have a zero dc component. It was found that the derivative of a sine function raised to a high order integer power provided the best results.

Fortran computer code was written to implement the finite difference equations described above. Loops were used to advance the field components throughout the problem space for each time step. Spatial resolution was set at 1 cm for both coordinates. The time step was set just below the minimum required by the Courant stability criteria [4]. The results presented in the following sections are based on this model. This approach can be modified to incorporate additional features such as interactions with a conducting gas, including nonlinear constitutive relations. Also, a magnetic current conductor can be used as a source that would allow for the interactions of the RF emitter and its environment (i.e. radiation resistance and reactance), or other nearby sources can be developed.

4. ANALYSIS OF MEASUREMENTS

4.1 Antenna Range Measurements

Measurements of RF emissions from the light bulb were conducted on the NIST antenna measurement range. In this environment, the light bulb was located 103 cm (using a nonconducting tripod) above a flat surface constructed of wire mesh and sheet metal, which for the frequencies of interest can be considered a perfectly conducting ground plane. Measurement equipment was located in a tunnel below the surface (Figure 6). There were no buildings or other objects (which are likely to cause interference) in the immediate vicinity of the test site.

The selection of field probes and the measurement strategy were based on the geometry and RF characteristics of the light bulb. The cylindrical symmetry of the light bulb components combined with the frequency of operation implied that the light bulb RF source would function primarily as a magnetic dipole. In this case, the near field electromagnetic emissions can most readily be measured with "shielded" loop antennas which strongly reject the electric field coupling and stray currents induced on the shielded cable connected to the antenna. The 12-in calibrated loop antenna was used to obtain an absolute measurement and the 6-cm loop antenna was used to obtain field amplitudes at a variety of spatial locations. These antennas were described in Section 2.3.

Records of the measured power in the fundamental band for each spatial location using the 6-cm loop antenna are given in the Appendix. Table 1 summarizes the measurements in terms of the maximum measured power in the fundamental band using a spectrum analyzer resolution bandwidth of 1 kHz. It should be noted that all of the results presented in this section are measured or calculated with respect to a 1-kHz bandwidth.

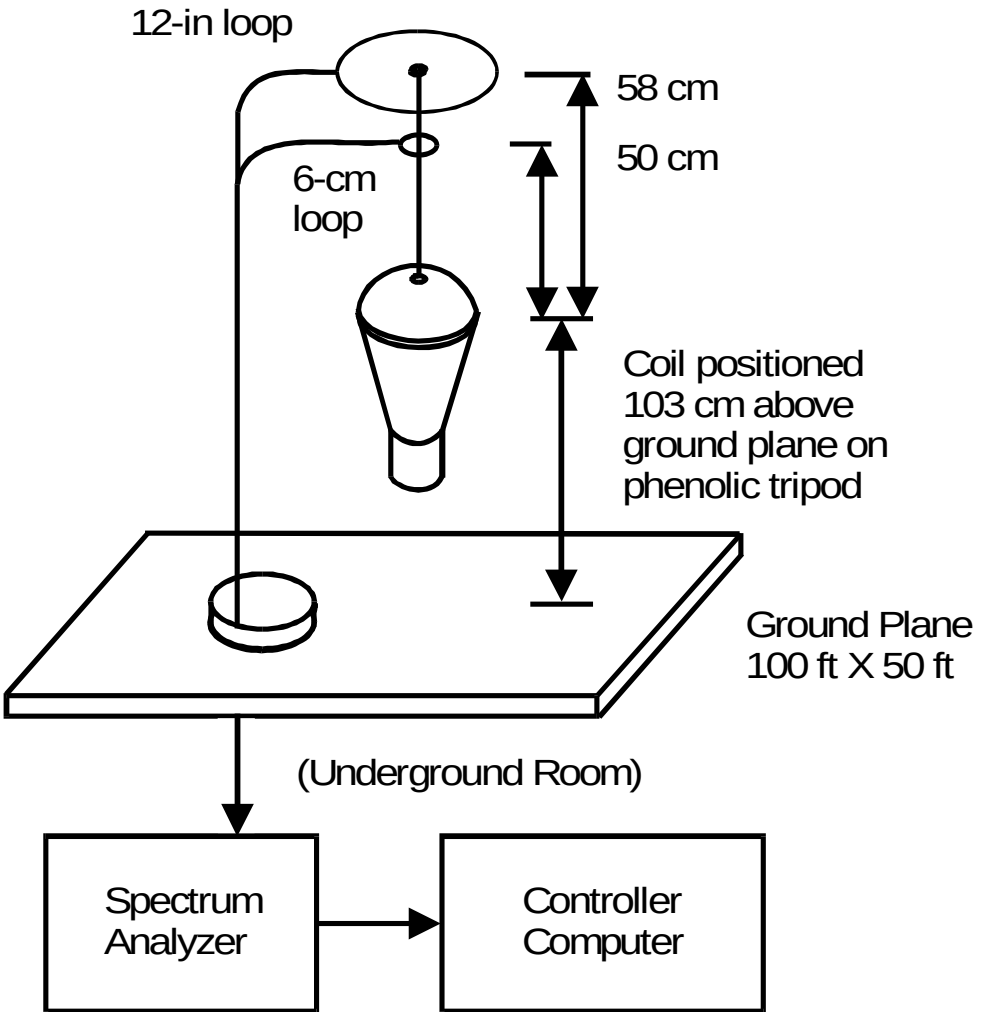

Figure 6. Antenna range measurement setup.

Three 6-cm loop antenna orientations were used in these measurements. These orientations are defined in terms of the cylindrical coordinates illustrated in Figure 7 as follows:

$\hat{z}$ orientation--the loop area unit normal is equal to the z axis unit vector,

$\hat{r}$ orientation--the loop area unit normal is equal to the r axis unit vector, and

$\hat{\phi}$ orientation--the loop area unit normal is equal to the ϕ axis unit vector.

Thus, each power measurement corresponds to the cylindrical component of the average magnetic field intercepted by the loop. In Table 1, the maximum measured power in a 1-kHz bandwidth is given for each loop orientation. Spherical coordinates (R, θ illustrated in Figure 7) are used to indicate the spatial location of the measurement. Figure 7 shows the relationship between the cylindrical and spherical coordinates, and the RF light bulb.

Table 1. Maximum Measured Power (6-cm Loop Antenna, 1-kHz Resolution Bandwidth) in the Fundamental Band at Various Near Field Locations

	Maximum power for various loop antenna orientations and R = 0.5m (dBm)			Maximum power for various loop antenna orientations and R = 1.0 m (dBm)		
θ	$\hat{z}$	$\hat{r}$	$\hat{\phi}$	$\hat{z}$	$\hat{r}$	$\hat{\phi}$
0	-55	-97	--	-75	-112	--
π/4	-72	-58	-88	-90	-78	-90
π/2	-63	-80	-87	-81	-94	-89
3π/4	-69	-61	-89	-93	-77	-90
π	-60	-89	--	-107	-92	--

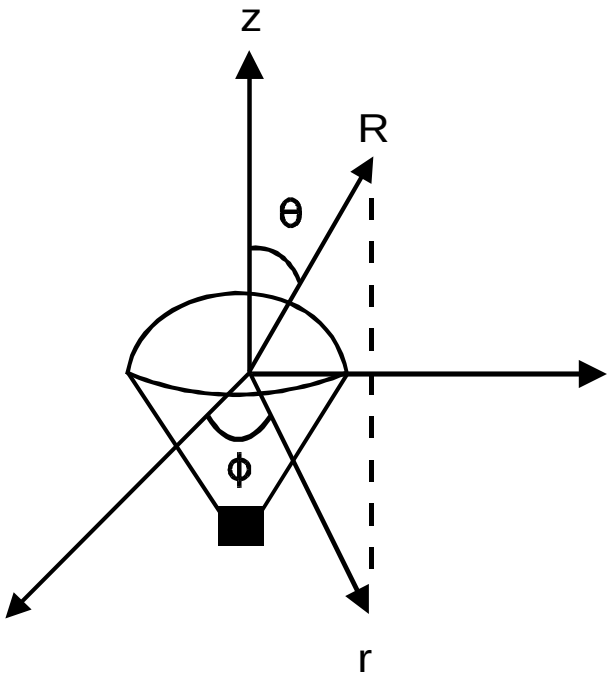

Figure 7. Definition of coordinate systems for the light bulb.

Next, the measured RF emissions in terms of the average magnetic field strength (H_{avg}) and those predicted by the model described in Section 3 were compared. The magnetic field components corresponding to the power measurements given in Table 1 were calculated using the following expression:

$$H_{avg} = AFH + P_a - 13 \quad (dB\ A/m) \tag{10}$$

where H_{avg} is proportional to the flux enclosed by the loop, AFH is the antenna factor, and P_a is the measured power in *dBm*. The measured and modeled values of H_{avg} in dB relative to the absolute values of H_{avg} at spherical coordinates R = 0.5 m and $\theta = 0$ for the $\hat{z}$ and $\hat{r}$ antenna orientations are given in Table 2. These results show good agreement which validates both the near field measurement techniques and the assumption that the RF light bulb can be modeled as a magnetic dipole source.

Due to the size of the loop, the measurements at $\theta = 0$ and π are expected to have a greater uncertainty than measurements at other angles.

Measurements made with the calibrated 12-in loop antenna in conjunction with the Green's function calculated from the simulation model were used to determine the effective magnetic dipole moment of the RF light bulb coil as described below. This result is useful since a simple magnetic dipole model can be used to easily calculate both near and far field emissions for complicated geometries and light bulb arrangements.

For this measurement, the light bulb RF source was placed at the center of the 12-in loop. Using Faraday's law and Equation 10, the tangential electric field (in decibels) at the loop is

$$E_\phi = 20\log_{10} F_{MHz} + 20\log_{10} R + AFH + P - 1 \quad (dB\ V/m) \tag{11}$$

Table 2. Comparison of Relative Measured and Calculated Field Strengths Using the Simulation Model

Spherical angle θ (radians)	Relative field strength at R = 0.5 m				Relative field strength at R = 1.0 m			
	$H_{avg}\ \hat{z}$ (dB)		$H_{avg}\ \hat{r}$ (dB)		$H_{avg}\ \hat{z}$ (dB)		$H_{avg}\ \hat{r}$ (dB)	
	Measured	Modeled	Measured	Modeled	Measured	Modeled	Measured	Modeled
0	0	0	−37	−42*	−19	−20	−61*	−67*
$\pi/4$	−16	−17	−3	−3	−33	−35	−22	−22
$\pi/2$	−7	−8	−22	−25	−24	−26	−40	−39
$3\pi/4$	−14	−14	−5	−6	−41	−38	−21	−22
π	−3	−5	−41	−34**	−45	−52	−58	−47**

*based on model resolution, $H_{avg}\ \hat{r}$ is calculated at $\theta = 0.003\pi$

**based on model resolution, $H_{avg}\ \hat{r}$ is calculated at $\theta = 0.997\pi$

where 2.5 MHz is used as a nominal value for F_{MHz}, R = 0.1524 m (the distance from the source to the loop), AFH is the antenna factor (−3 dB A/V/m at 2.5 MHz), and P is the measured power density in dBm. The maximum inband measured power is about 1 dBm (from Figure A-27) and hence, E_ϕ = −11.4. Using the Green's function obtained from the model, the calculated ratio of the magnetic dipole moment to the electric field at R = 0.1524 m and θ = 0 at 2.5 MHz was −28.6 dB; hence, the equivalent magnetic moment of the RF light bulb is −40 dB (Am^2). The corresponding magnetic induction in the RF coil (represented by a magnetic current in the model) is given by

$$B = \frac{\mu_\circ m}{\pi a^2 \ell} = 1 \times 10^{-4} (T) \qquad \textbf{(12)}$$

where m is the magnetic moment, a is the radius of the coil, and ℓ is the length of the coil.

The 12-in calibrated loop antenna in conjunction with the fields predicted by the model were also used to calibrate the measurements made with the 6-cm loop (performance factors based on manufacturer's design specifications are provided; however the loop itself was not calibrated). From Equation 11 the ratio of the circumferential electric fields is related to the antenna factors as follows:

$$E_\phi^{(2)} - E_\phi^{(1)} = 20 \log_{10} \frac{R^{(2)}}{R^{(1)}} + AFH^{(2)} - AFH^{(1)} + P^{(2)} - P^{(1)} \quad (dB) \qquad \textbf{(13)}$$

where the superscripts are used to distinguish quantities related to the two loop antennas and E_ϕ is the circumferential field along the loops illustrated in Figure 8a. First, the small loop was placed at the location of the maximum field strength at the top of the light bulb (5 cm above the coil as illustrated in Figure 8) where the maximum measured power (from Figure A-28) was $P^{(2)}$ = 13 dBm. This was compared to the 12-in loop antenna measurement with the RF source at the center of the loop where the measured power density was (from Figure A-28) $P^{(1)}$ = 1 dBm. Using these results in Equation 13 gives

$$AFH^{(2)} = E_\phi^{(2)} - E_\phi^{(1)} - 0.9 \quad (dB\ A/V/m). \qquad \textbf{(14)}$$

The ratio of the circumferential fields was calculated with the model and for the configuration given in Figure 8a was found to be 20.2 dB; hence, $AFH^{(2)}$ = 19.3.

The same technique was applied to the geometry shown in Figure 8b with loop antennas above and coaxial with the RF source. For this measurement, the 12-in loop antenna was 58 cm above the source and $P^{(1)}$ = −34 dBm (from Figure A-29). The 6-cm loop was 50 cm above the source with a measured power density of $P^{(2)}$ = −55 dBm (from Figure A-1); hence,

$$AFH^{(2)} = E_{\phi}^{(2)} - E_{\phi}^{(1)} + 32.1 \ (dB \ A/V/m). \qquad \textbf{(15)}$$

The ratio of the circumferential fields was calculated with the model, and for the configuration given in Figure 8b it was −10.1 dB; hence, $AFH^{(2)}$ = 22. From Figure 3, the performance factor for the 6-cm loop antenna is about 85 dB at 1 MHz with a slope of −23 dB/decade; hence, the published electric field performance factor at 2.5 MHz is 77.2 dB and the magnetic field performance factor is about $AFH^{(2)}$ = 24, which is somewhat higher than the calculated factors.

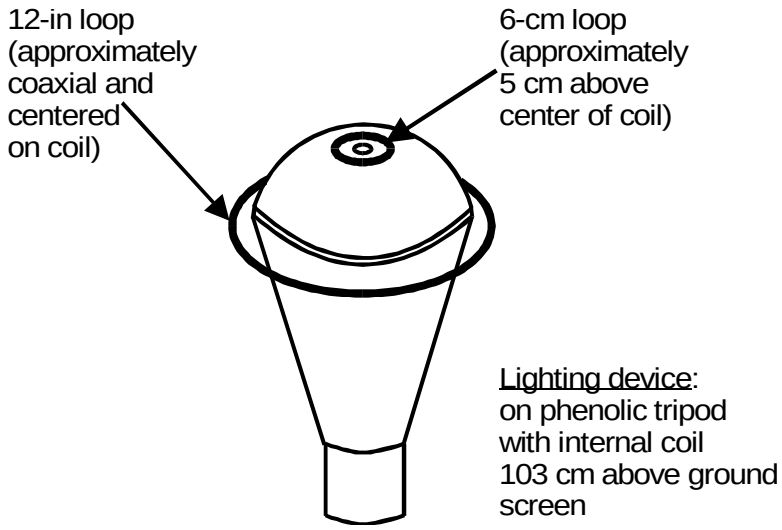

Figure 8a. Antenna locations for measuring the dipole moment.

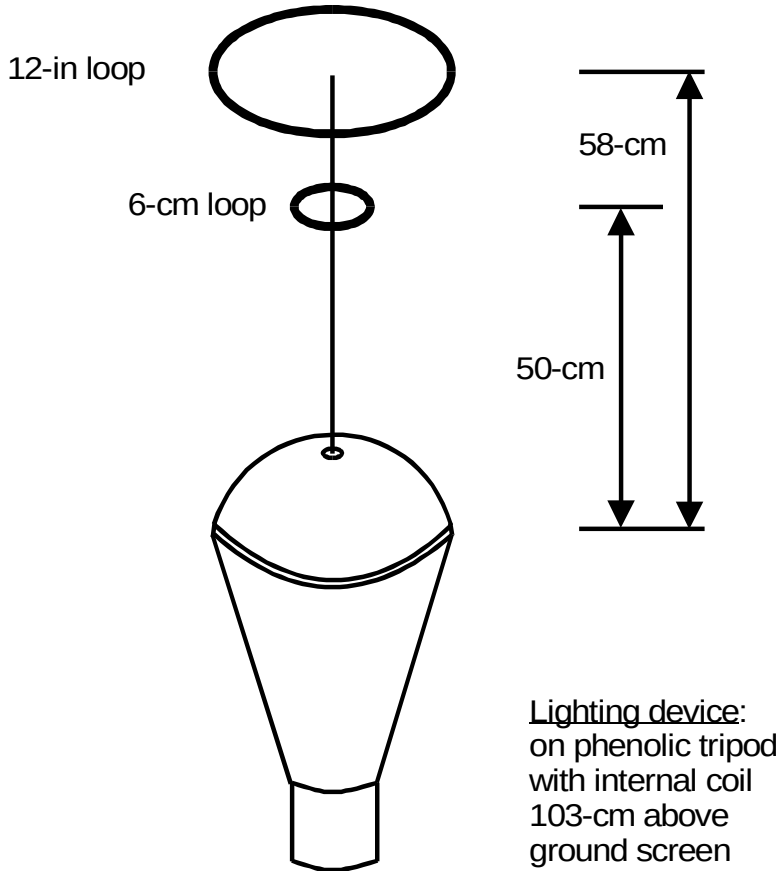

Figure 8b. Calibration geometry for 6-cm loop.

A series of electric field measurements were made using the EMCO ball probe described in Section 2. These measurements were much more sensitive to the local environment. For example, up to 10 dB variations in power were observed depending on the proximity of personnel to the probe. This was not observed when using the loops. Field variations in terms of spherical angle (θ) were relatively small, while doubling the distance from the source (increasing R from 0.5 to 1.0 m) resulted in power decreases on the order of 10 dB. Typically, peak power measured 0.5 m from the source was about −95 dBm (see Figure A-30) and peak power measured 1.0 m away was in the range of −105 dBm or less (see Figure A-31). The fact that signal strength was not a strong function of spherical angle with the ball probe is likely due to induced currents on the shielded cable. Based on this experience, it was assumed that while the ball probe may provide an estimate of the electric field strength at a given distance, it is not useful for measuring field variations as a function of spherical angle (θ).

Based on the manufacturer's specified performance factor (about 81 dB at 2.5 MHz), the measured electric field strength at 0.5 m from the source is −27 dB V/m, and at 1.0 m is about −37 dB V/m. These values are somewhat higher than the maximum electric field strength (E_ϕ) predicted by the model and loop measurements given in Table 3. Given the doubts about the actual performance of

the ball probe in this setting (i.e., rejection of currents induced on the cable shield), the uncertainty in the performance factor is likely much greater than with the loop probe.

Because of the inherent symmetry of the source and the frequency of operation, it is expected that the magnetic field lines are predominantly in the plane(s) containing the axis of the RF source coil and the electric field is predominantly circumferential. This is consistent with the $\hat{\phi}$ measurements given in Table 1, which are relatively low and show only slight variations with changes in spatial location. In the case of a strong vertically oriented electric dipole moment, it would be expected that the circumferential magnetic field strength at 0.5 and 1.0 m would change by about 12 dB.

Maximum predicted fields in the fundamental band (nominally 2.5 MHz) based on model calculations and measurements using the 6-cm loop antenna are given in Table 3. The model is driven by a magnetic current source corresponding to a magnetic moment of −40 dB Am^2; an antenna factor of 22 dB was used to correct the 6-cm loop measurements from Table 1 (shown in parentheses). The results are in terms of the maximum magnetic (dB A/m) or electric (dB V/m) field strength in a 1-kHz bandwidth.

Due to the uncertainty (described above) associated with the electric field probe, electric fields presented are those predicted by the model. As expected, the strongest fields are at $\pi/2$ and the electric field decreases by 12 dB at 1 m. This is consistent for the near field of a magnetic dipole. Divergence from true dipole behavior is indicated by the lack of symmetry (about $\theta = \pi/2$) in both the measured and calculated results. In particular, at R = 0.5 m, this asymmetry is not likely due to the ground since the image-produced magnetic field is at least 16 dB below the field produced by the actual source. Both measured and calculated fields at spherical angles of 0 and π have a greater uncertainty than other angles.

Table 3. Calculated and Measured Field Strengths

	Field strength at R = 0.5 m			**Field strength at R = 1.0 m**		
θ	H_z dB (A/m)	H_r dB (A/m)	E_ϕ dB (V/m)	H_z dB (A/m)	H_r dB (A/m)	E_ϕ dB (V/m)
0	-45 (-46)*	-81 (-87)	-69	-64 (-66)	-106 (-103)	-79
$\pi/4$	-61 (-63)	-48 (-49)	-35	-78 (-81)	-67 (-69)	-47
$\pi/2$	-51 (-54)	-67 (-71)	-33	-69 (-72)	-85 (-85)	-45
$3\pi/4$	-59 (-60)	-50 (-52)	-37	-86 (-84)	-66 (-68)	-51
π	-48 (-51)	-86 (-80)	-74	-90 (-98)	-102 (-83)	-111

*Measured values are in parentheses.

4.2 TEM Cell Measurements

NIST has developed a technique for complete characterization of emissions from an unknown source using a TEM cell [1, 2]. The light bulb emissions were measured using the NIST TEM cell as part of the overall measurement strategy.

The TEM cell is an enclosed coaxial structure and is used at frequencies that excite only the fundamental mode. The source is placed in the center of the cell and is characterized by determining the coupling for six different orientations with respect to the TEM field. The Lorentz Reciprocity Theorem for perfectly conducting waveguide walls is applied to relate the unknown source represented by a combination of both electric and magnetic dipole moments to the amplitudes of electric and magnetic basis functions used to describe the field structure of the fundamental mode.

For the purposes of calculating electric and magnetic dipole moments, the light bulb was placed in a local Cartesian coordinate system. Here the z coordinate corresponds to the axis of symmetry of the light bulb (cylindrical coordinate z shown in Figure 7). The x and y coordinates were chosen arbitrarily (with respect to the light bulb). The measured equivalent dipole moments for each coordinate (nominally at 2.5 MHz) are given in Table 4.

Table 4. Electric and Magnetic Dipole Moments Measured with a TEM Cell (1-kHz Resolution Bandwidth)

	x-axis dipole	**y-axis dipole**	**z-axis dipole**
Electric Dipole moment (Am)	not detectable	7.5831×10^{-7}	3.0932×10^{-6}
Magnetic Dipole moment (Am^2)	not detectable	9.5470×10^{-4}	3.9428×10^{-3}

As expected, the electric dipole moments are quite small and the magnetic dipole moment is primarily aligned along the z axis. The smaller component along the y axis is likely due to imperfect alignment of the source along the z axis and/or nonsymmetrical attributes of the light bulb.

The dipole moments given above are based on the assumption that the electromagnetic fields detected in the TEM cell are due to ideal electric and magnetic dipoles. On the other hand, the dipole moment calculated above using the model and 12-in loop measurement (0.01 Am^2) is the effective dipole moment of the RF coil inside the light bulb; it does not assume that the unit as a whole acts like an ideal dipole source. To compare these results we calculated the magnetic dipole moment that yields the same electric field as detected by the 12-in loop centered around the light bulb (−11.4 dBm or 0.27 V/m) using the near field approximation for the electric field due to a magnetic dipole (m):

$$e_{\phi} = \frac{2\pi \times 10^{-7}}{r^2} m f. \quad \textbf{(16)}$$

At 2.5 MHz, the equivalent dipole moment was found to be 3.87×10^{-3}, which is in excellent agreement with the TEM cell results.

The total radiated power density can be calculated directly from the equivalent dipole moments, which gives 1.1687×10^{-9} W in a 1-kHz bandwidth. The results of the TEM cell measurements confirm that for the fundamental frequency (nominally 2.5 MHz), the contribution of electric dipole moments to the total power radiated are not significant and the magnetic dipole is primarily oriented along the axis of symmetry of the light bulb.

Figures A-55 and A-56 show the total radiated power from about 1 - 20 MHz, based on the TEM cell measurements. Figure A-55 shows the fundamental and two prominent harmonics at about 5 and 7.5 MHz. A subharmonic was also noted at about 1.2 - 1.3 MHz. In this case, the measurements were performed using a hybrid junction with a range of 2 - 2000 MHz. This junction was replaced with one suitable for use below 2 MHz in order to obtain a more accurate measurement of this feature. The resulting radiated power is shown in Figure A-56. Interestingly enough, while the fundamental and first two harmonics are present with nearly the same amplitude, the subharmonic has disappeared. The cause of this seemingly spurious event was not determined. Due to the small amplitude (−118 dBm), this event (if present) would not have been detected in the series of measurements using the H-field and E-field probes.

The curved appearance of the noise floor in these figures is an artifact of the total radiated power calculation for the assumed dipole sources (i.e., for a dipole source, wavelength is a divisor in the power calculation). Also, the dual spikes at 5 MHz in Figure A-55 most likely are due to frequency drift during the series of measurements.

4.3 Harmonics and Other Measurements

Both a magnetic field probe and an electric field probe were used to measure harmonics. Since harmonics can be produced by the spectrum analyzer, a 10-dB attenuator was used to discriminate between internally and externally produced harmonics. This was accomplished by placing the attenuator at the input to the analyzer (in which case externally generated signals should drop by 10 dB).

Figures A-32 and A-33 show harmonics detected with the 12-in loop centered around the light bulb (Figure A-32 is without attenuation, Figure A-33 is with attenuation). The 10-dB attenuation test indicates that harmonics between 5 and 13 MHz are generated by the light bulb.

Since electric dipole moments are more likely to be generated at higher frequencies, the electric field ball probe was also used to detect harmonics. Background scans (light off) are included with the data. Figure A-34 shows emissions detected between 125 and 375 MHz and Figure A-36 shows the background. Insertion of the 10-dB attenuator indicated that these emissions are generated by the light bulb (Figure A-35). The measurements were made with the probe next to the light bulb. Figure A-37 shows the result of moving the probe to a distance of 1 m from the light bulb. The emissions no longer are present. Additionally, scans over a broad range of frequencies were collected with the probe located at a distance of 1 m from the source (Figures A-38)A-41). Other than the fundamental emission from the light bulb (Figure A-41 at 2.5 MHz), no significant signals were detected using this probe at 1 m.

A series of measurements were made to determine variations in field strength as a function of the cylindrical coordinate ϕ. These measurements were accomplished using the 6-cm loop (using the $\hat{z}$ and $\hat{\phi}$ orientations) at horizontal distances of 0.5 and 1.0 m from the source. No significant variations were observed.

Measurements of the conducted current were performed indoors using a wide band current monitor (Model 110 manufactured by Pearson Electronics, Inc). The correction factor for this device is 0.1 V/A. For this measurement, the light bulb was placed in a shield room to prevent coupling of the RF emissions to the current monitor. The current monitor was placed on the power cord outside of the shield room. Results of this measurement are shown in Figure A-42. Scans of the emissions near 60 kHz using the 12-in loop are shown in Figure A-43. No significant emissions were noted.

Measurements of the time domain envelope were performed indoors using the 12-in loop centered on the light bulb. Figures A-44 through A-49 show the results of these measurements and the calculated amplitude probability distributions. The emissions near 2.5 MHz as a function of the input voltage are shown in Figures A-50 through A-54.

5. SUMMARY AND CONCLUSIONS

The major electromagnetic radiation components of this device appear in Table 3 of this report. The field strengths near the device are quite small. Also, the magnetic fields decay following the inverse cube of the distance law as expected in the static zone. However, to achieve these results, it was necessary to devise a system of measurement that eliminates interactions between the radiation device and the proximity of measuring probes. To fully evaluate and eliminate these interactions, a simulation model was developed which permitted calculation of the field at any point of interest. The agreement between the calculated and measured results should be noted. The associated equations are provided in Section 3. The utility of the model is significant in predicting the near field of any RF EMI radiating system that can be represented by such a simulation and utilizing a varied probe technique analogous to that described in this report. The methodology described in this report will be of general interest to those involved in EMI/EMC analysis since such work often involves near field measurements and potential complex interactions between probing methods and the device under test. Simulation models

such as the one used here are essential to understanding what the measurements represent, the prediction of emissions, and the development of measurement techniques.

A number of harmonics were measured and the results are shown in the Appendix. Of note are the emissions in the 150 to 450 MHz band. On the antenna range, these were detected primarily using the EMCO ball probe located next to the light bulb. When the probe was moved out a meter, the emissions were no longer detectable. These emissions were also detectable with the loop, although, when 10 dB of attenuation was inserted, the emissions dropped below the noise level. The emissions in this band also were detectable in the TEM cell; however, because the cell is not calibrated above 150 MHz, meaningful field levels could not be obtained. The capability of measuring the total radiated power in this band does exist. However, it requires the use of a more elaborate test chamber. Such measurements are advisable in order to accurately assess the total radiated power in this band.

6. REFERENCES

[1] M.T. Ma, and G.H. Koepke, “A method to quantify the radiation characteristics of an unknown interference source,” NBS Technical Note 1059, Oct. 1982.

[2] G.H. Koepke, M.T. Ma, and W.D. Bensema, “Theory and measurements of radiated emissions using a TEM cell,” NIST Technical Note 1326, Jan. 1989.

[3] K.S. Yee, “Numerical solution of initial boundary value problems involving Maxwell's equation in isotropic media,” *IEEE Trans. Ant. and Prop*., AP-14, No. 3, pp. 302-307, 1966.

[4] A.Taflove and M.E. Brodwin, “Numerical solution of steady-state electromagnetic scattering problems using the time-dependent Maxwell’s equations,” *IEEE Trans. Microwave Theory Tech*., Vol. MTT-23, No. 8, pp. 622-630, 1975.

[5] G.M. Smith, *Numerical Solution of Partial Differential Equations: Finite Difference Method*, Third Ed., Oxford: Clarendon Press, 1989.

APPENDIX: DATA SCANS

The purpose of this Appendix is to provide a record of the light bulb emission measurements. Most of the records given in the following figures are derived from spectrum analyzer scans using the setup shown in Figure 1. In general, power measurements are relative to a 1-kHz resolution bandwidth. The frequency span was typically set at 20 kHz with a sweep time of 300 ms.

The numbers in the appendix figure captions, for example #4-68, correspond to the data scan record number.

Figures A-1)A-26 are scans showing power measured using the 6-cm loop probe as described in Section 4 of this report. The coordinates and orientation of the probe, using the coordinate systems described in Section 4, are given in the figure captions.

Figures A-27)A-29 are the scans used for calibration described in Section 4 using both the 6-cm and the 12-in loop probes.

Figures A-30)A-31 show the scans obtained when the e-field ball probe was used.

Figures A-32)A-33 show the measured harmonics measured with the bulb in the center of the 12-in loop. Figure A-33 shows the results with a 10-dB attenuator inserted between the probe and the spectrum analyzer input.

Figures A-34)A-41 show the scans obtained using the e-field ball probe over a wide frequency range. The scan shown in Figure A-36 was taken with the light bulb switched off for reference.

Figure A-42 shows a scan obtained in the conducted current measurement.

Figure A-43 shows the 60-Hz response when the light bulb is at the center of the 12-in loop probe.

Figures A-44)A-49 show the time domain envelopes and corresponding amplitude distributions for measurements at the center frequency over a 1-kHz bandwidth.

Figures A-50)A-54 show how the radiated emissions vary with the light bulb voltage. Measurements were made with the bulb in the center of the 12-in loop.

Figures A-55)A-56 show the results of TEM cell measurements.

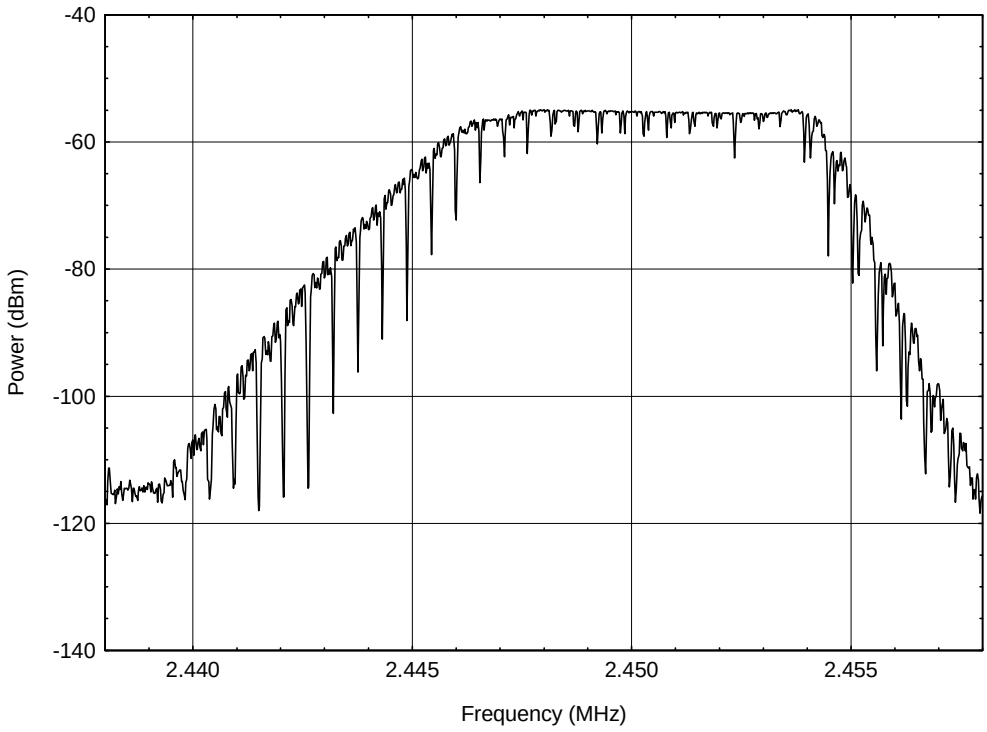

Figure A-1. Power measured with 6-cm loop probe axis parallel to z ($\hat{z}$), R = 0.5 m and 2 = 0 (#4-68).

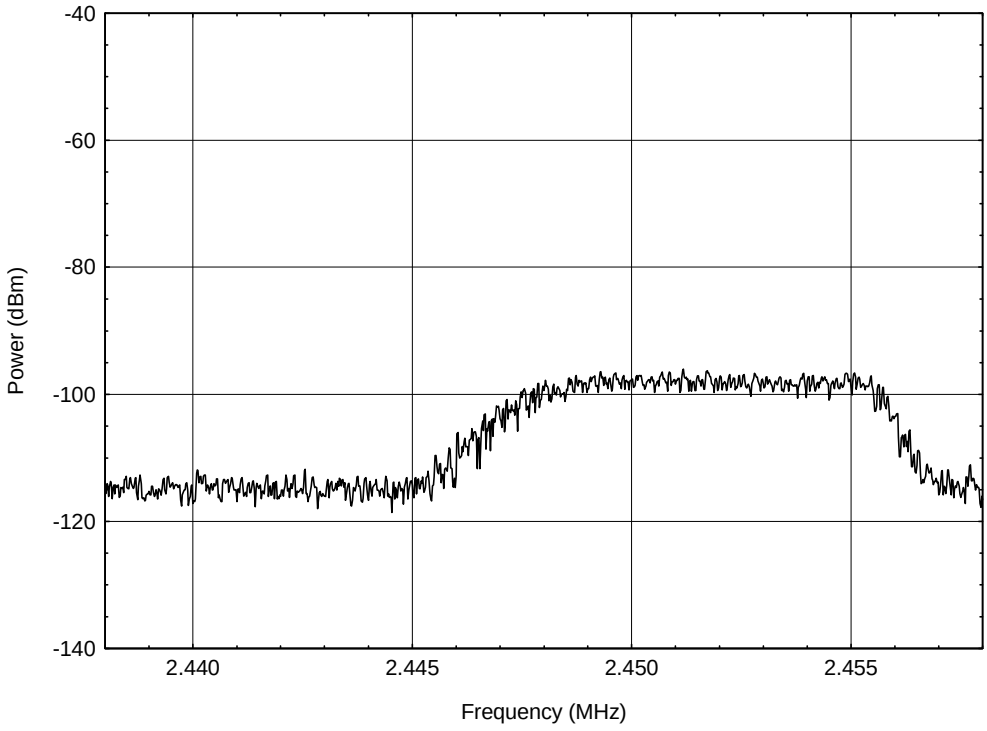

Figure A-2. Power measured with 6-cm loop probe axis parallel to r ($\hat{r}$), R = 0.5 m and 2 = 0 (#4-69).

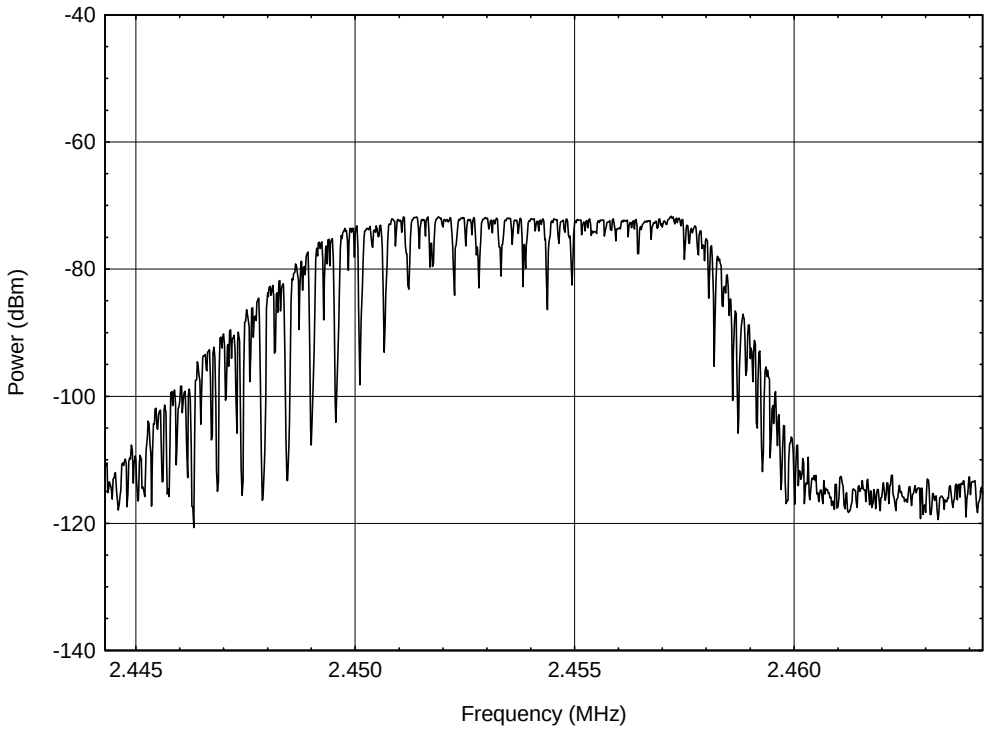

Figure A-3. Power measured with 6-cm loop probe axis parallel to z ($\hat{z}$), R = 0.5 m and 2 = B/4 (#4-59).

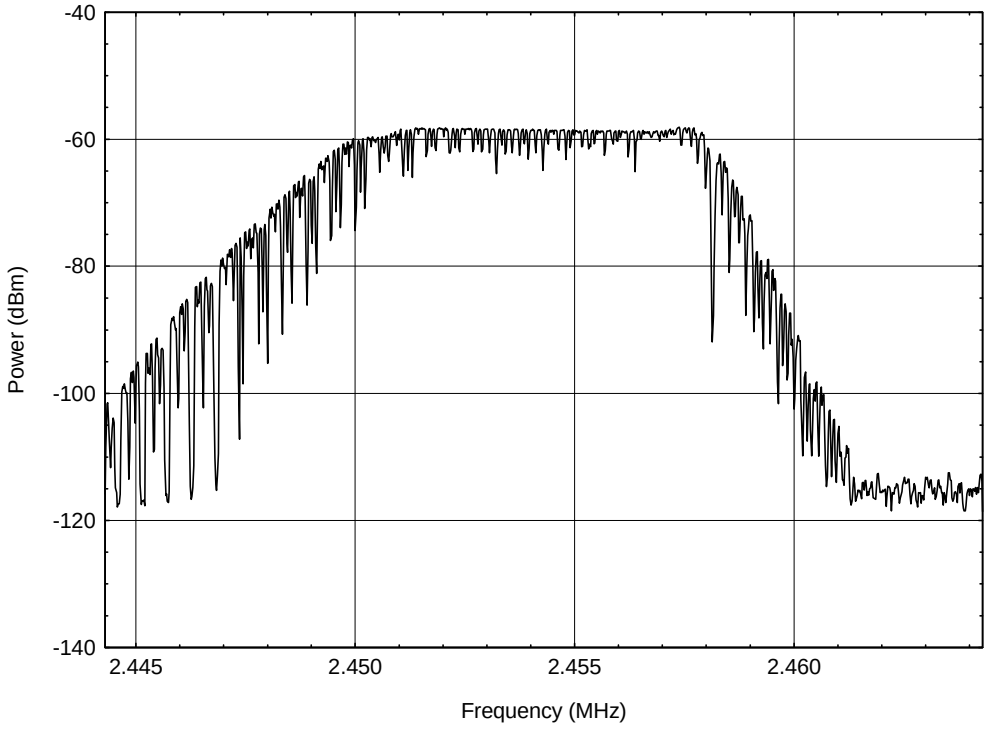

Figure A-4. Power measured with 6-cm loop probe axis parallel to r ($\hat{r}$), R = 0.5 m and 2 = B/4 (#4-60).

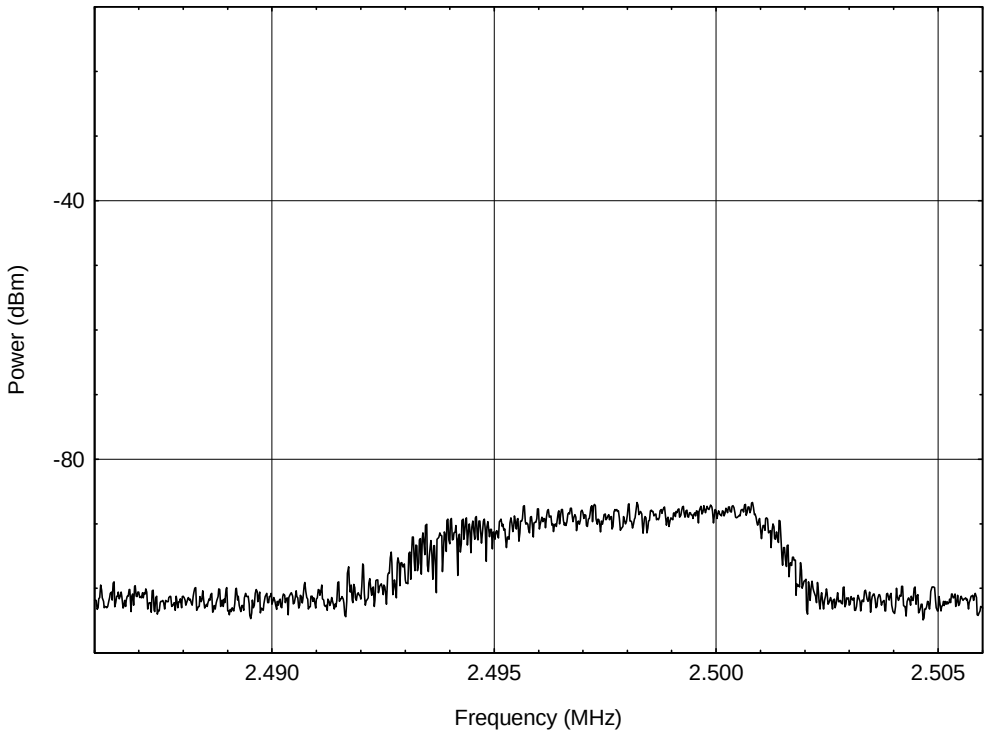

Figure A-5. Power measured with 6-cm loop probe axis parallel to $\hat{N}$, R = 0.5 m and 2 = B/4 (#5-44).

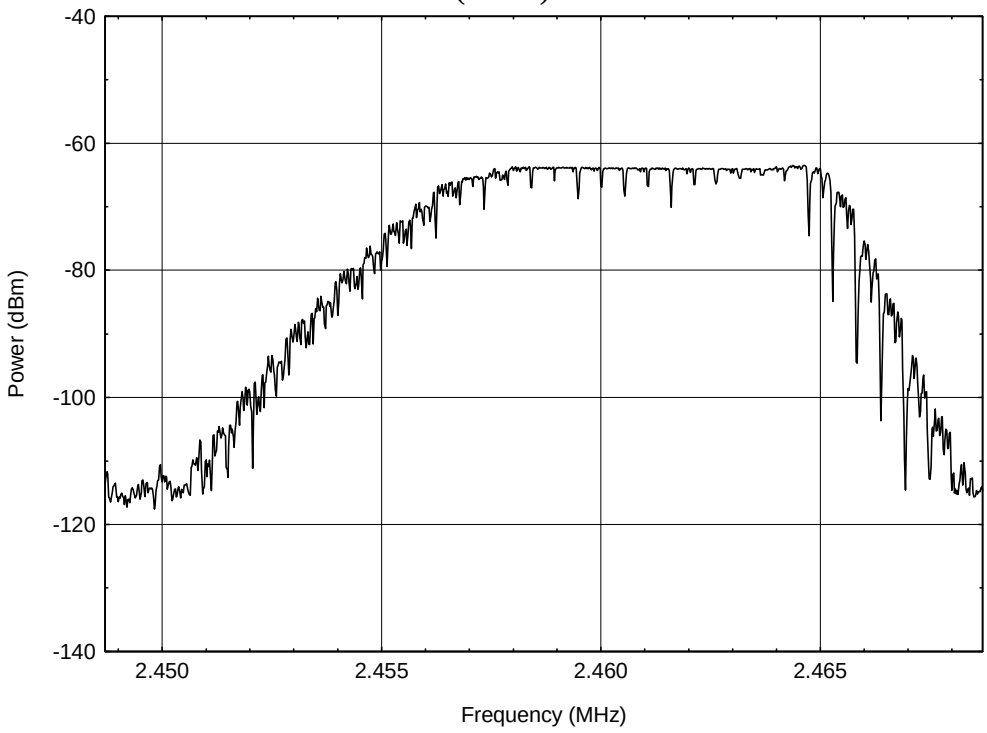

Figure A-6. Power measured with 6-cm loop probe axis parallel to $\hat{z}$, R = 0.5 m and 2 = B/2 (#4-31).

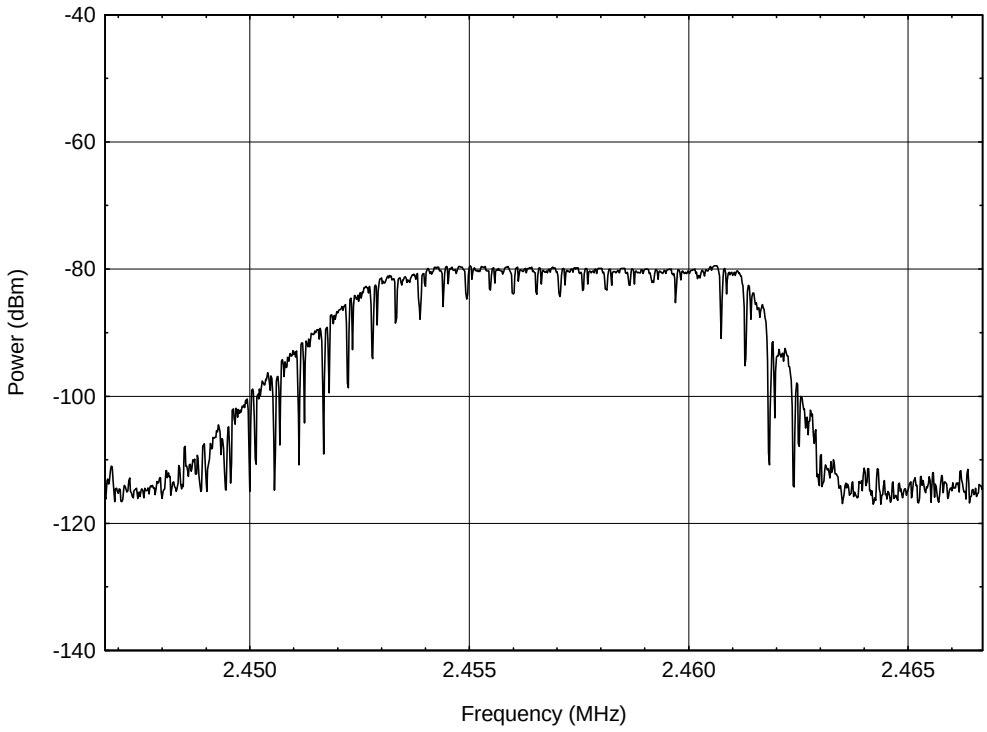

Figure A-7. Power measured with 6-cm loop probe axis parallel to r ($\hat{r}$), R = 0.5 m and 2 = B/2 (#4-42).

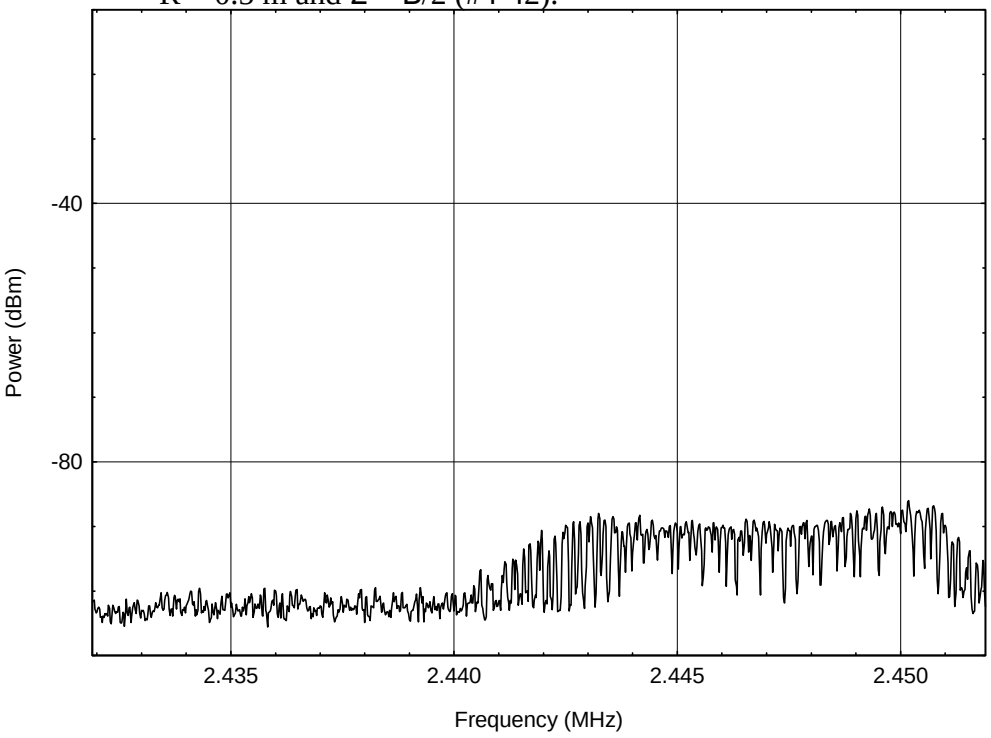

Figure A-8. Power measured with 6-cm loop probe axis parallel to N ($\hat{N}$), R = 0.5 m and 2 = B/2 (#5-56).

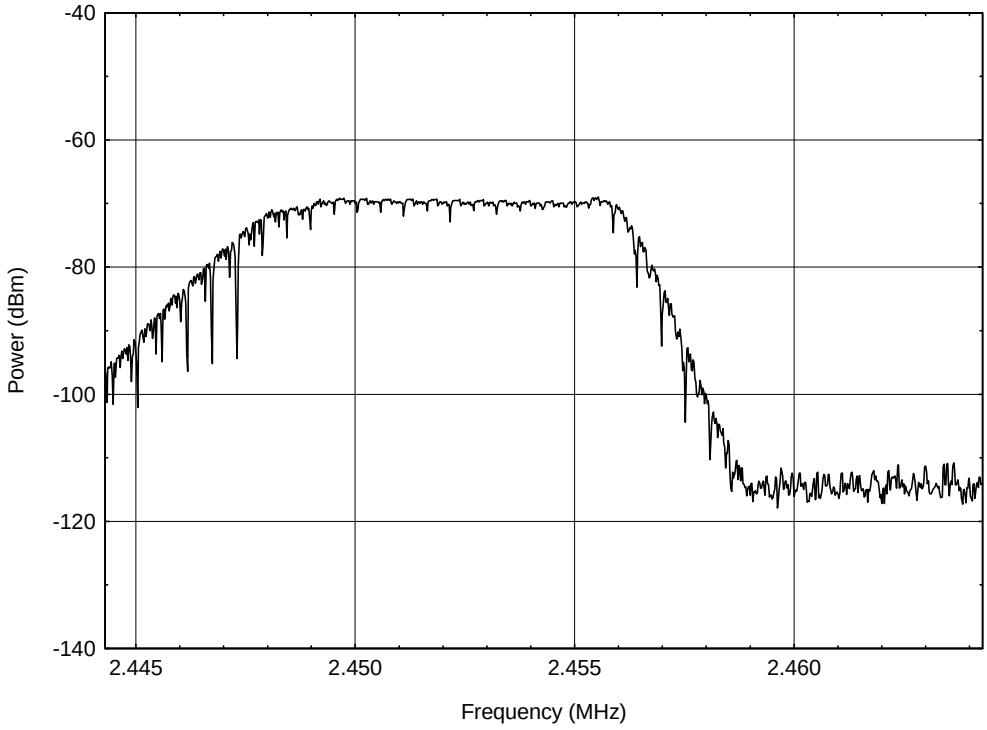

Figure A-9. Power measured with 6-cm loop probe axis parallel to z ($\hat{z}$), R = 0.5 m and 2 = 3B/4 (#4-53).

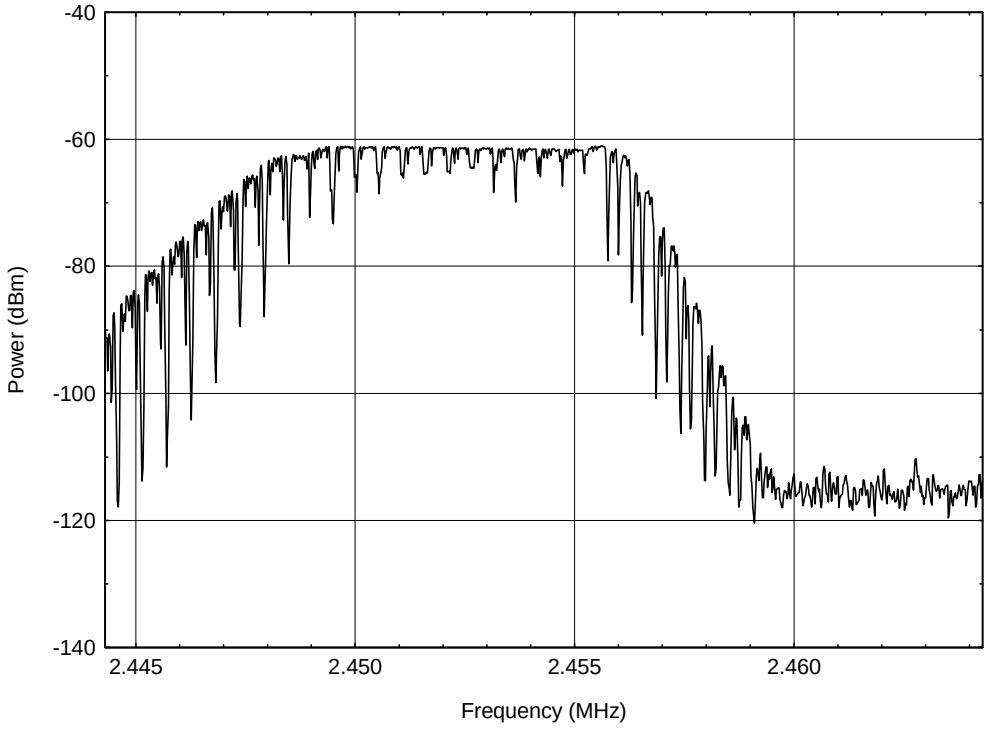

Figure A-10. Power measured with 6-cm loop probe axis parallel to r ($\hat{r}$), R = 0.5 m and 2 = 3B/4 (#4-54).

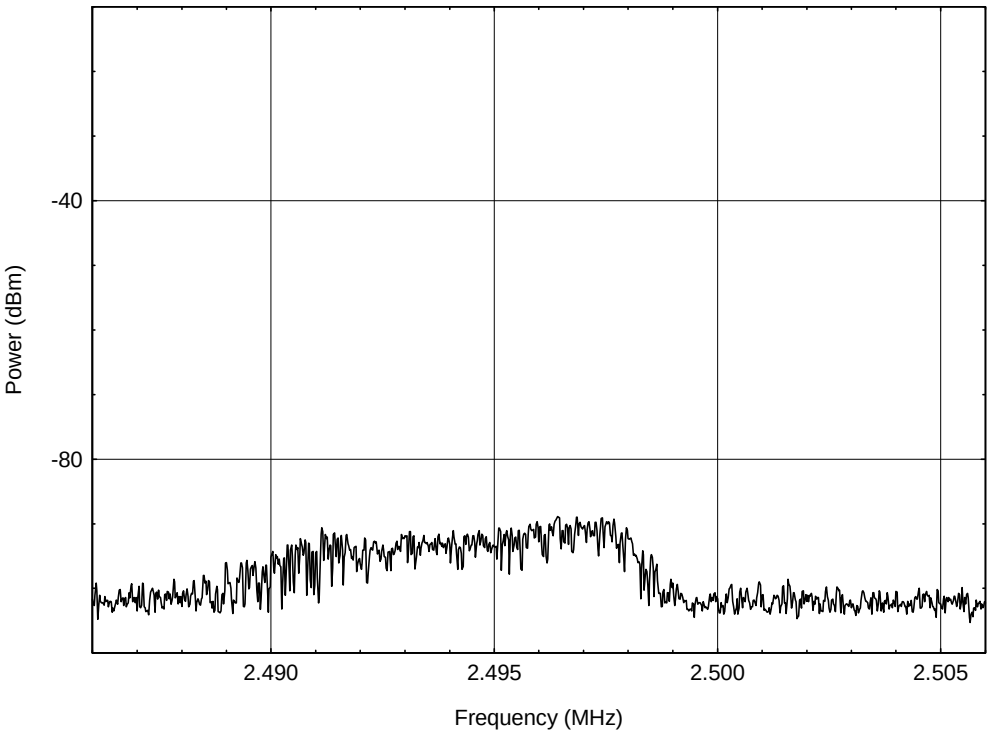

Figure A-11. Power measured with 6-cm loop probe axis parallel to $\hat{N}$, R = 0.5 m and $\theta = 3\pi/4$ (#5-42).

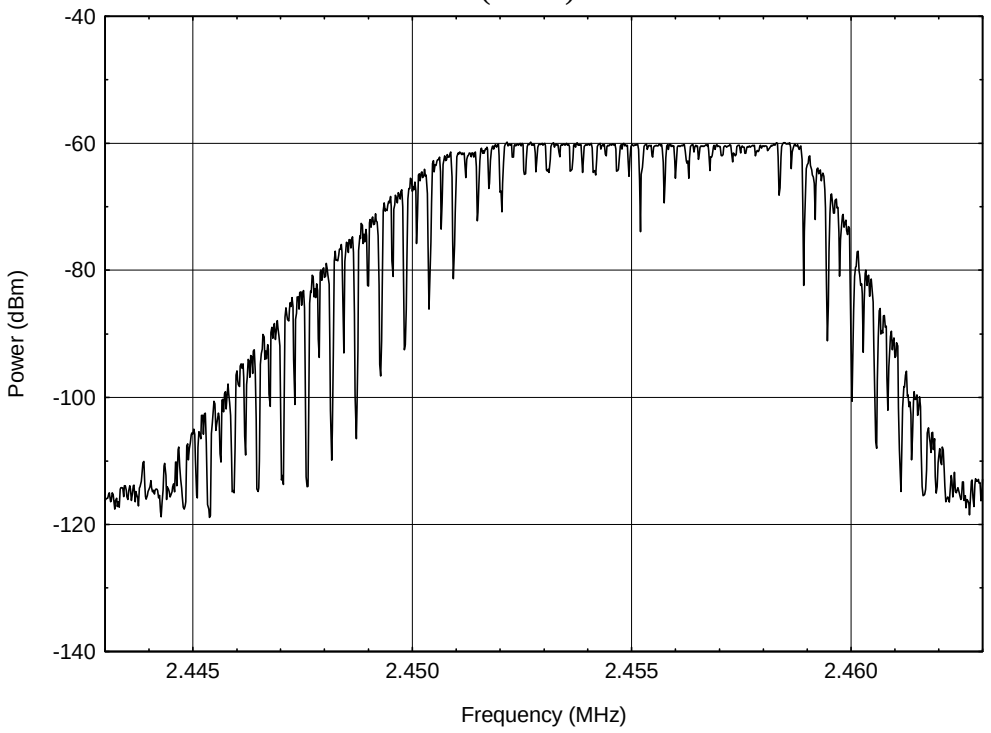

Figure A-12. Power measured with 6-cm loop probe axis parallel to $\hat{z}$, R = 0.5 m and $\theta = \pi$ (#4-70).

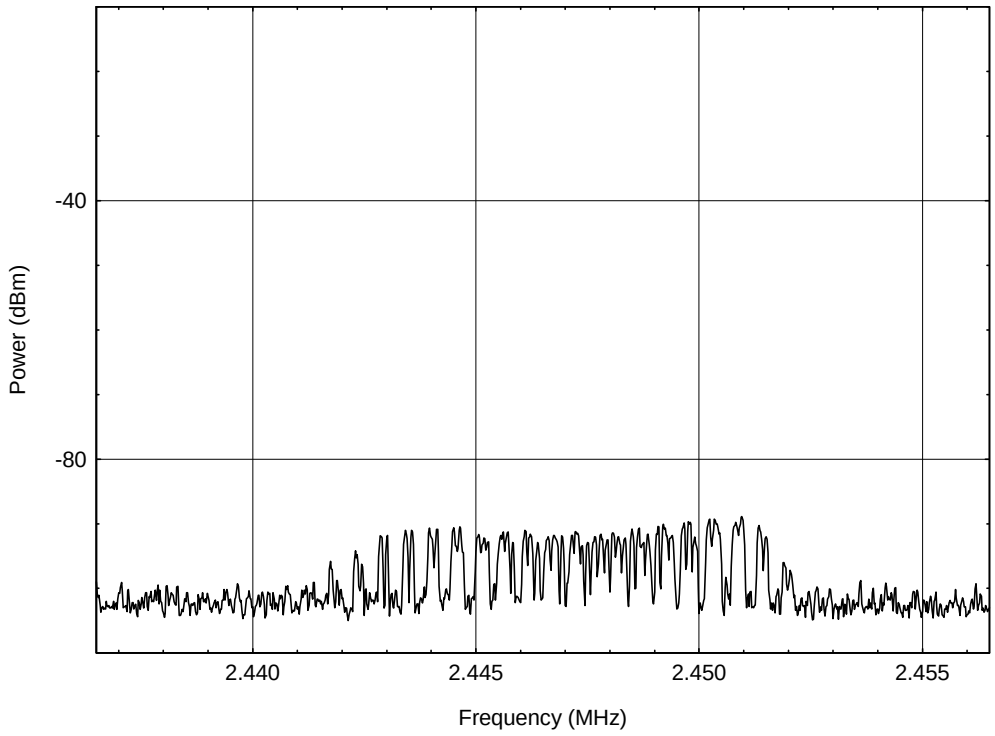

Figure A-13. Power measured with 6-cm loop probe axis parallel to r ($\hat{r}$), R = 0.5 m and 2 = B (#5-59).

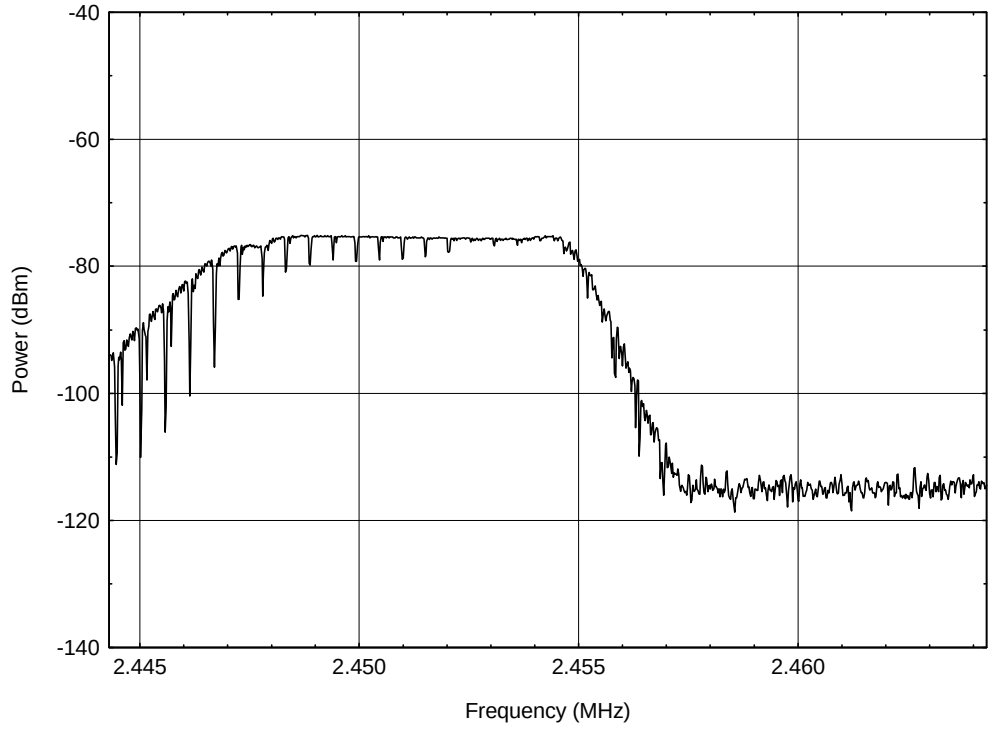

Figure A-14. Power measured with 6-cm loop probe axis parallel to z ($\hat{z}$), R = 1.0 m and 2 = 0 (#4-66).

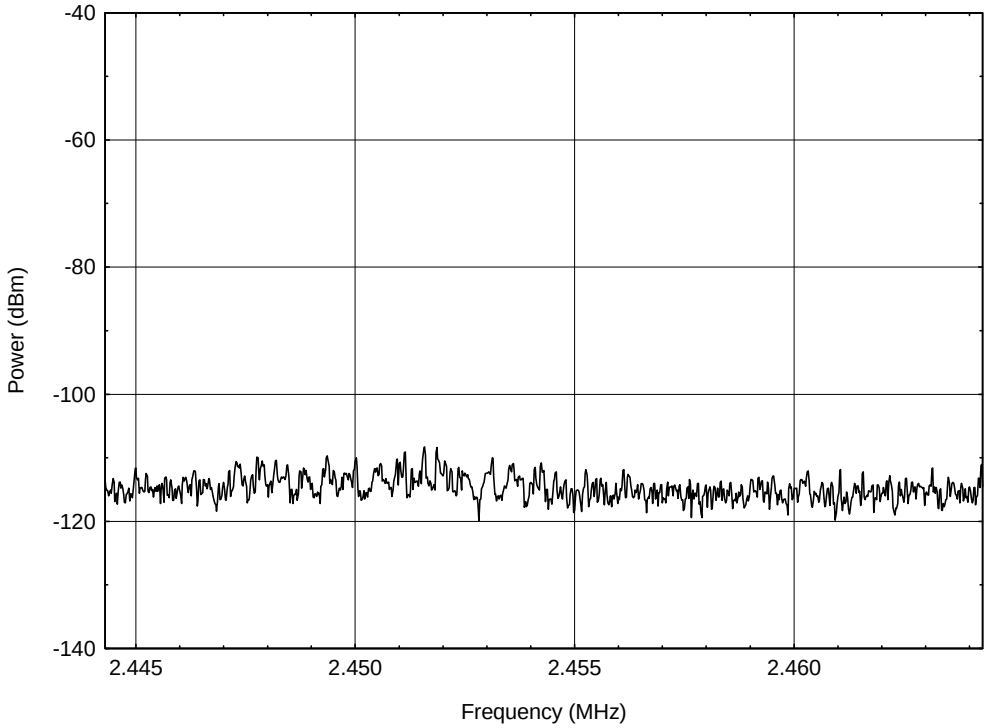

Figure A-15. Power measured with 6-cm loop probe axis parallel to r ($\hat{r}$), R = 1.0 m and 2 = 0 (#4-67).

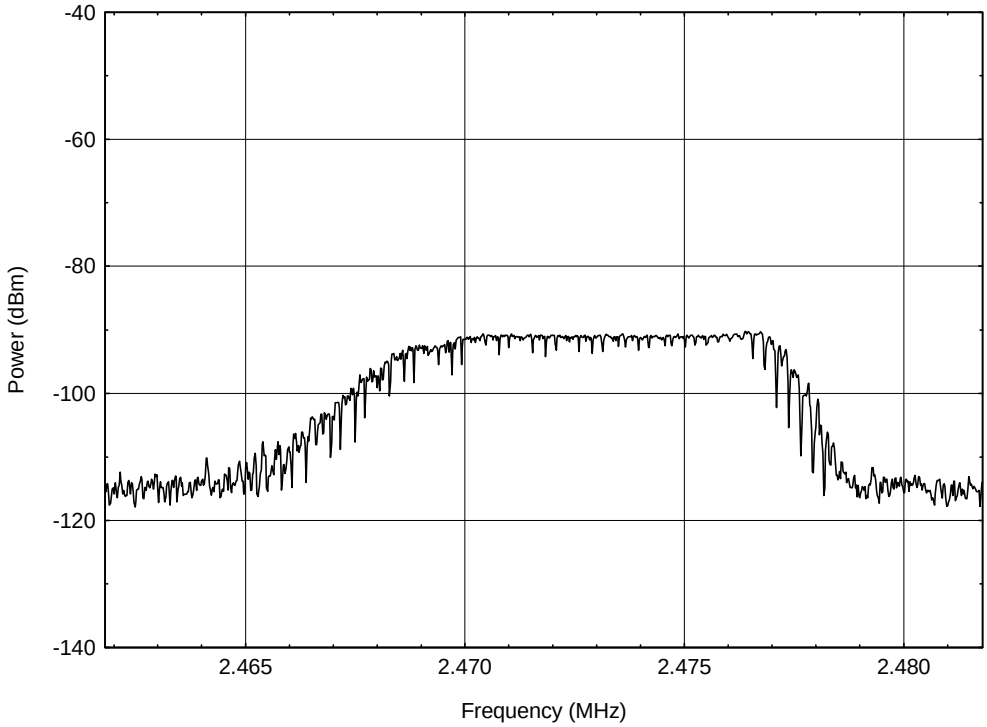

Figure A-16. Power measured with 6-cm loop probe axis parallel to z ($\hat{z}$), R = 1.0 m and 2 = B/4 (#4-36).

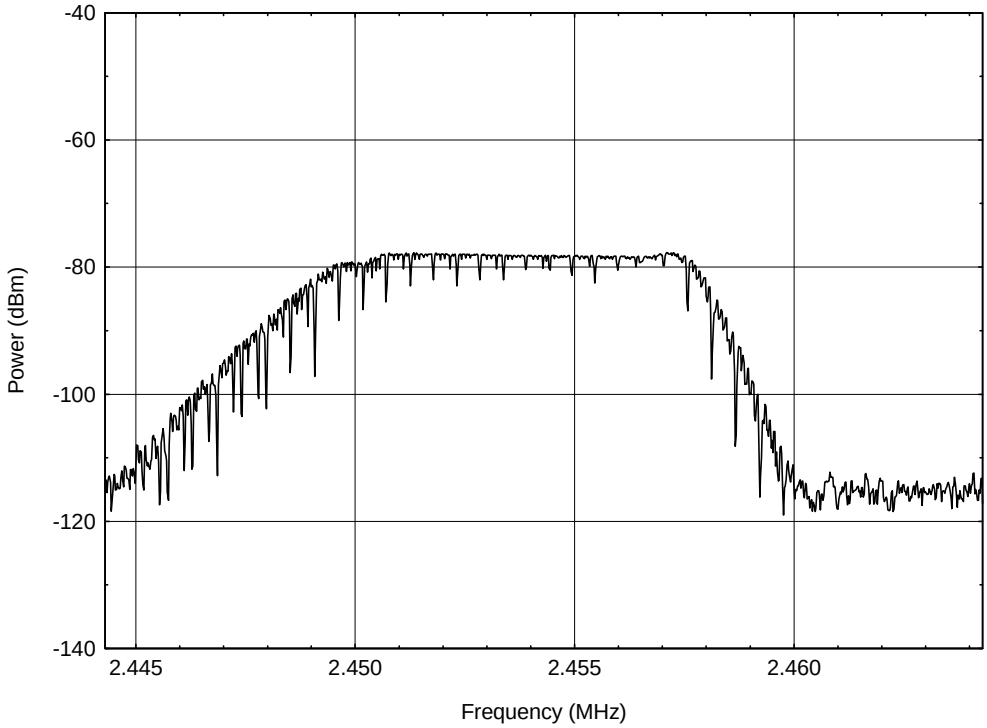

Figure A-17. Power measured with 6-cm loop probe axis parallel to r ($\hat{r}$), R = 1.0 m and 2 = B/4 (#4-62).

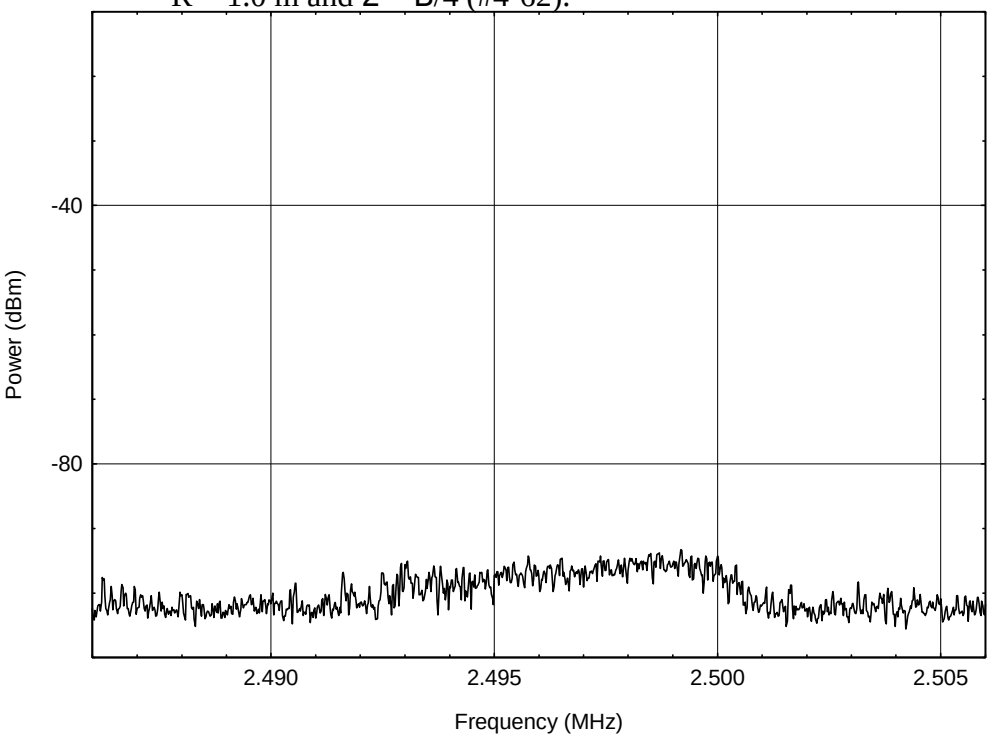

Figure A-18. Power measured with 6-cm loop probe axis parallel to N ($\hat{N}$), R = 1.0 m and 2 = B/4 (#5-45).

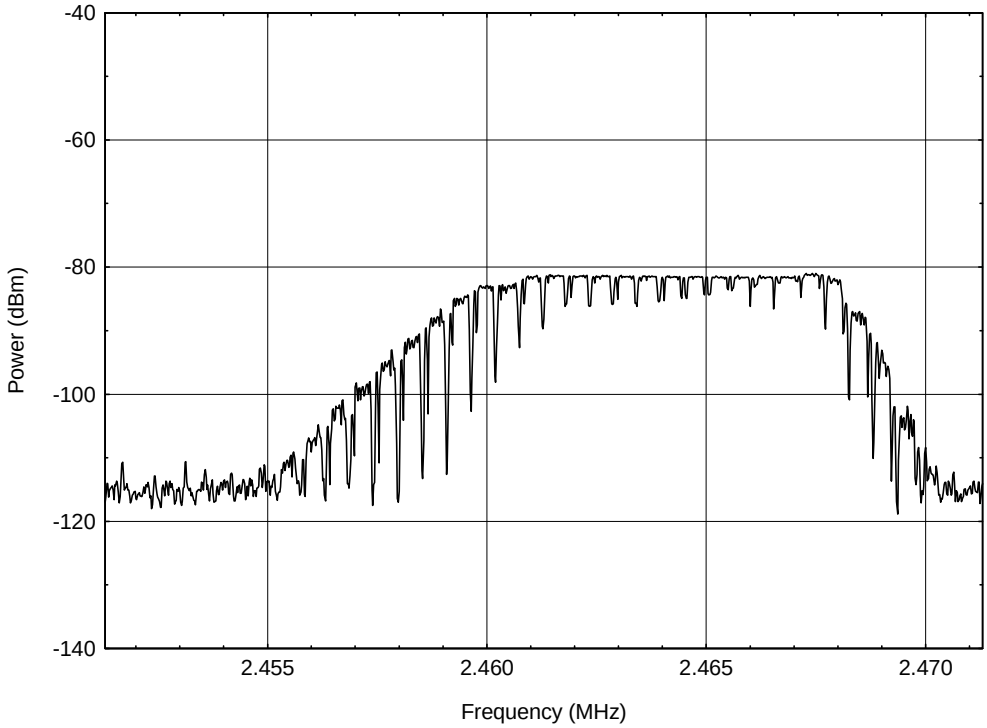

Figure A-19. Power measured with 6-cm loop probe axis parallel to z ($\hat{z}$), R = 1.0 m and 2 = B/2 (#4-32).

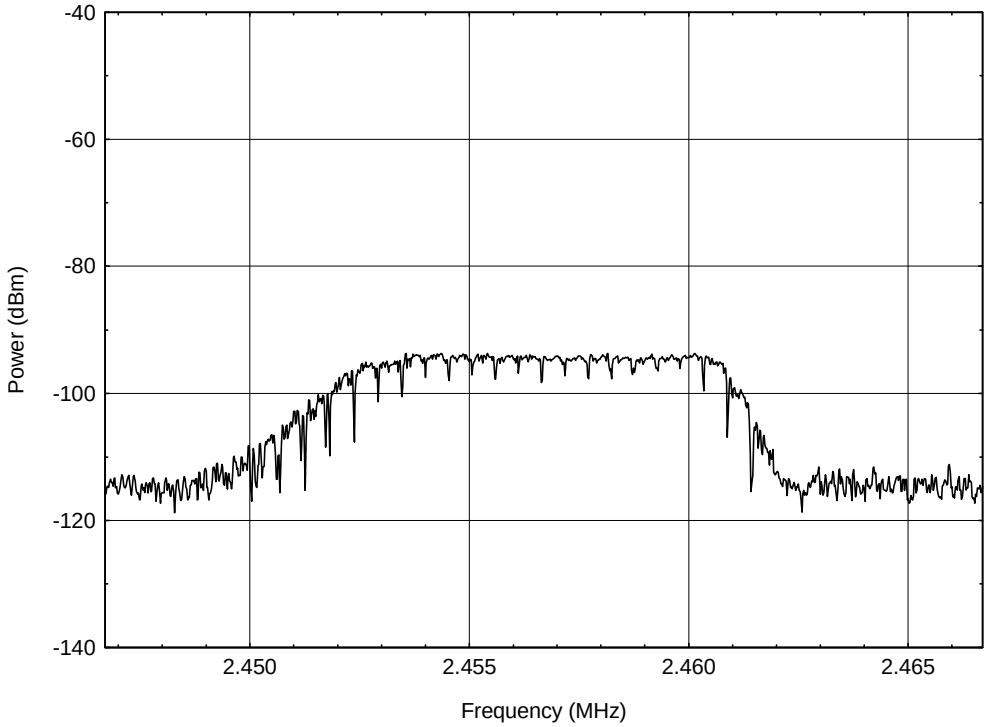

Figure A-20. Power measured with 6-cm loop probe axis parallel to r ($\hat{r}$), R = 1.0 m and 2 = B/2 (#4-43).

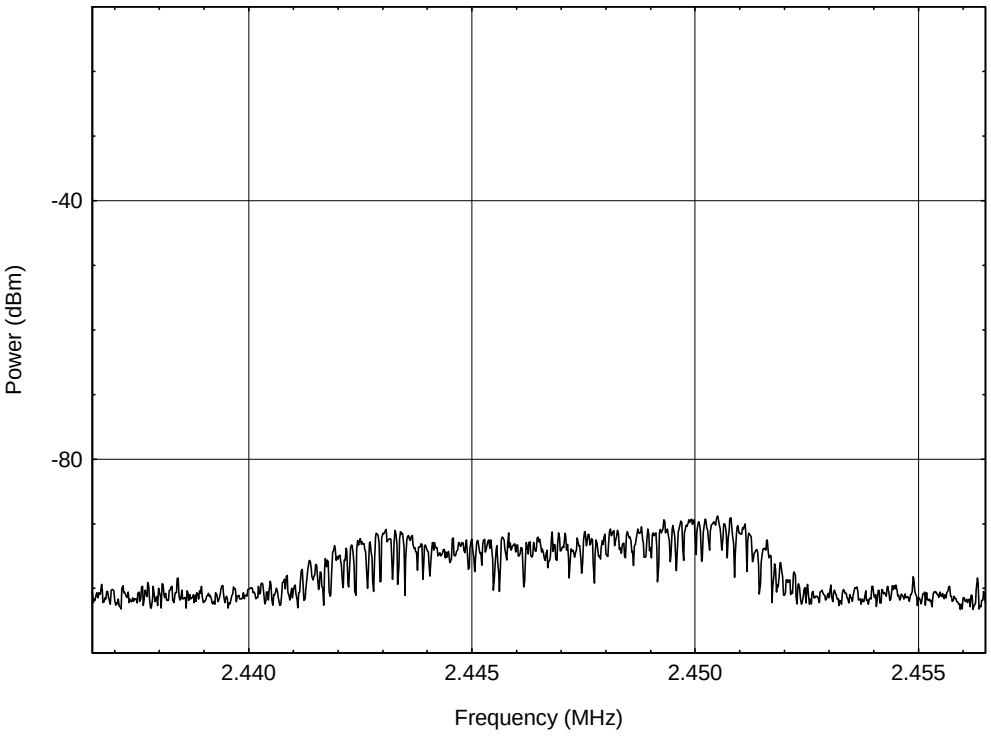

Figure A-21. Power measured with 6-cm loop probe axis parallel to N ($\hat{\mathsf{N}}$), R = 1.0 m and $\mathsf{2}$ = B/2 (#5-57).

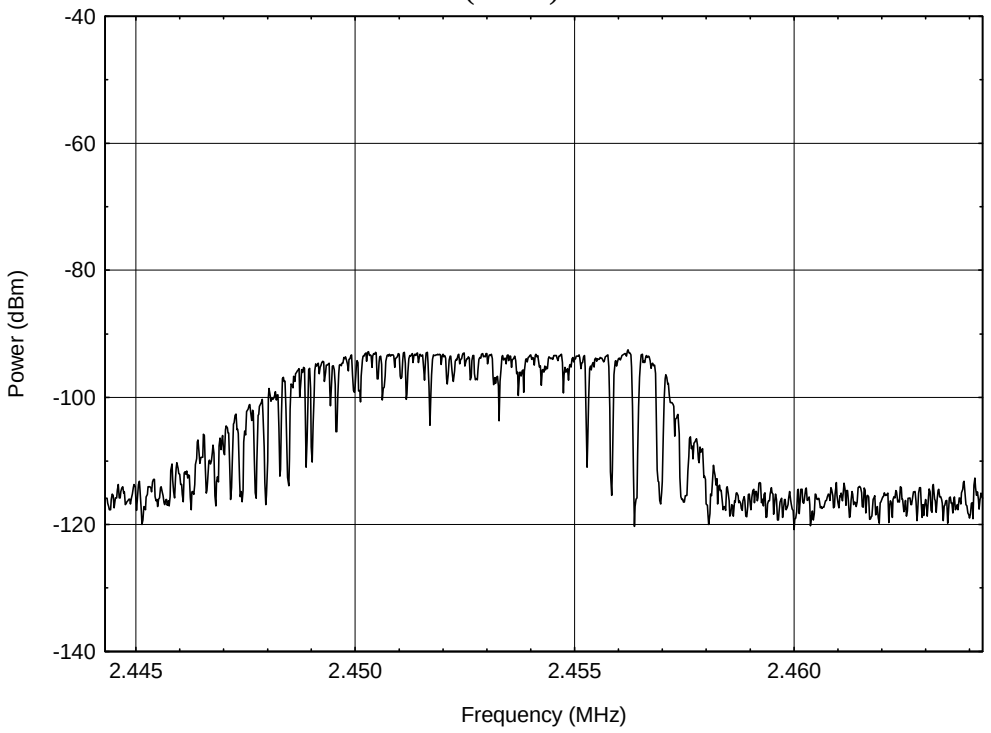

Figure A-22. Power measured with 6-cm loop probe axis parallel to z ($\hat{z}$), R = 1.0 m and $\mathsf{2}$ = 3B/4 (#4-55).

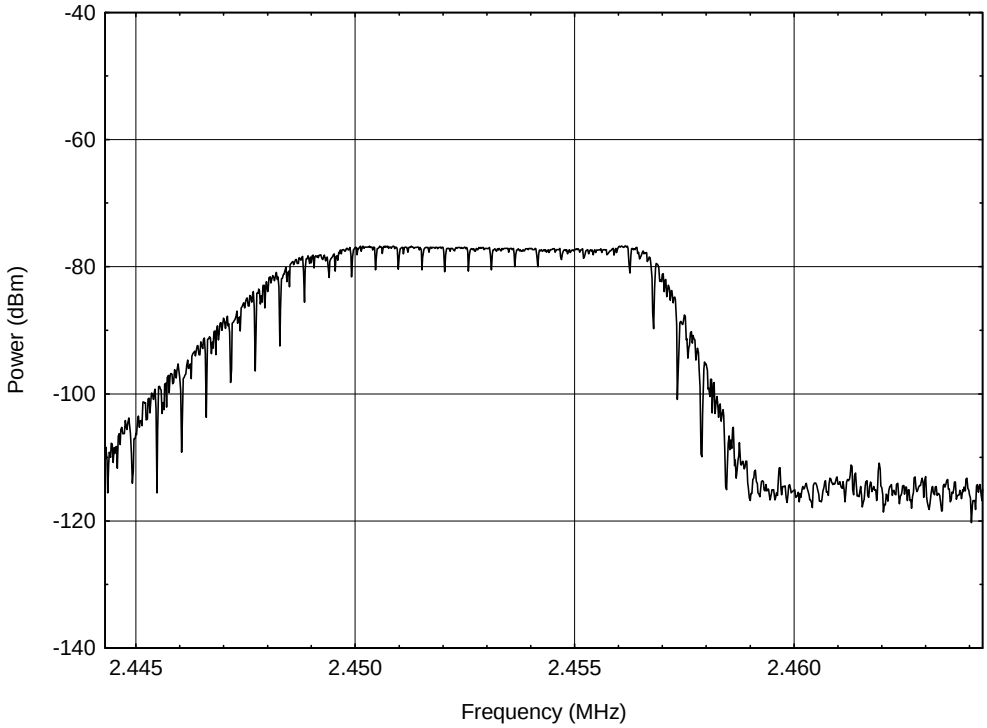

Figure A-23. Power measured with 6-cm loop probe axis parallel to r ($\hat{r}$), R = 1.0 m and 2 = 3B/4 (#4-56).

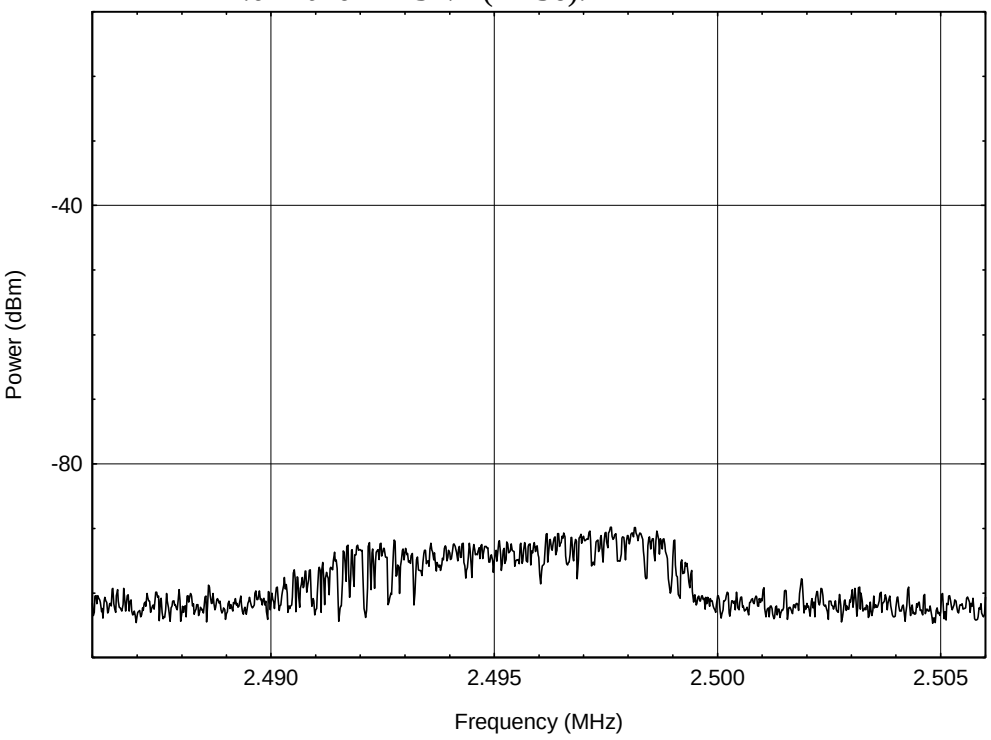

Figure A-24. Power measured with 6-cm loop probe axis parallel to N ($\hat{N}$), R = 1.0 m and 2 = 3B/4 (#5-43).

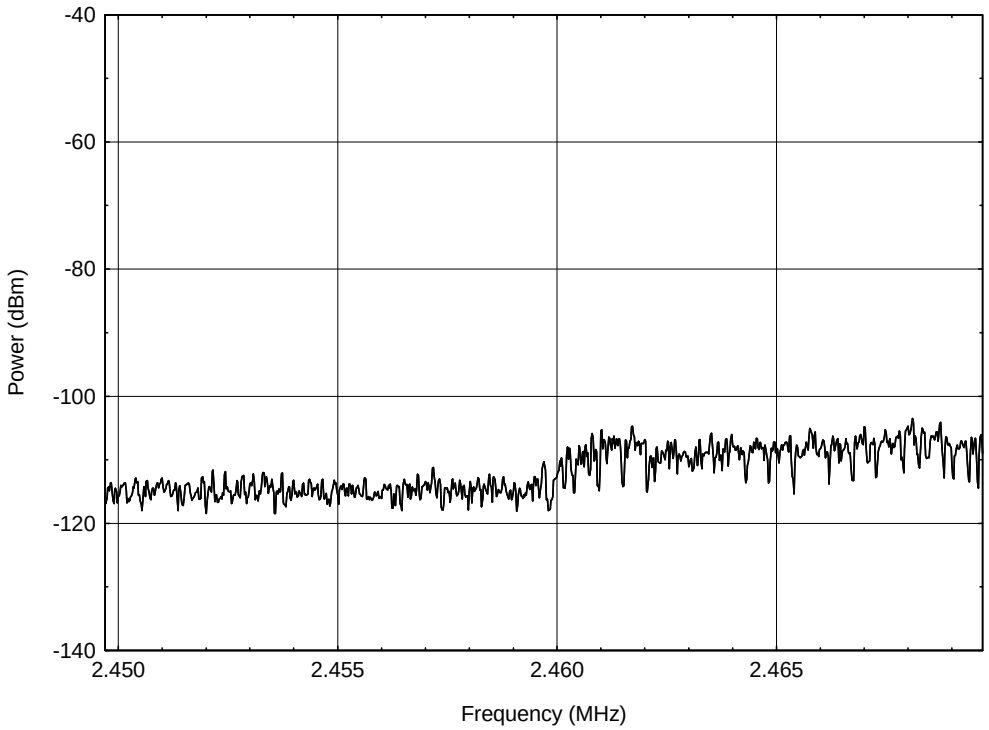

Figure A-25. Power measured with 6-cm loop probe axis parallel to z ($\hat{z}$), R = 1.0 m and 2 = B (#4-73).

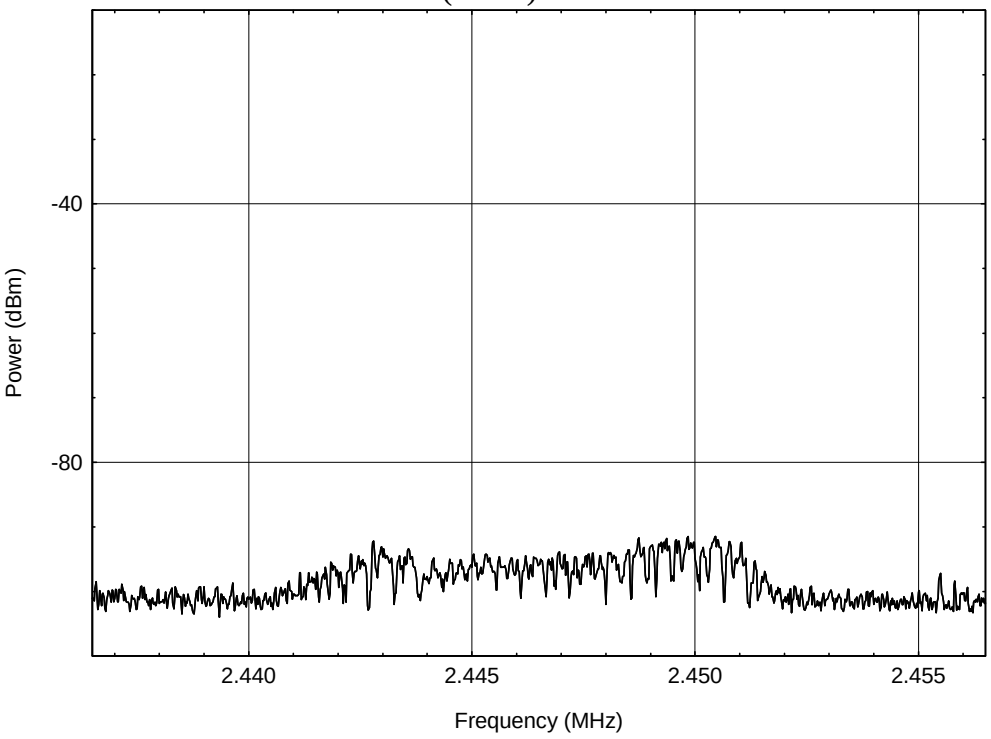

Figure A-26. Power measured with 6-cm loop probe axis parallel to r ($\hat{r}$), R = 1.0 m and 2 = B (#5-58).

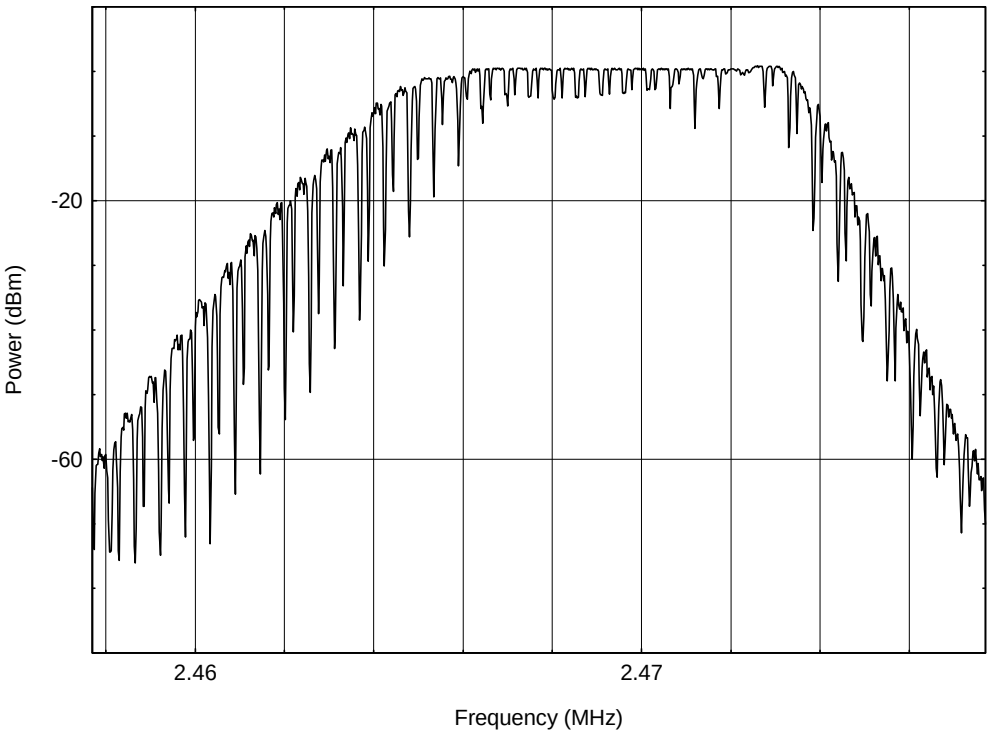

Figure A-27. Power measured with 12-in. loop probe axis parallel to z ($\hat{z}$), R = 1.0 m and 2 = B (#5-6).

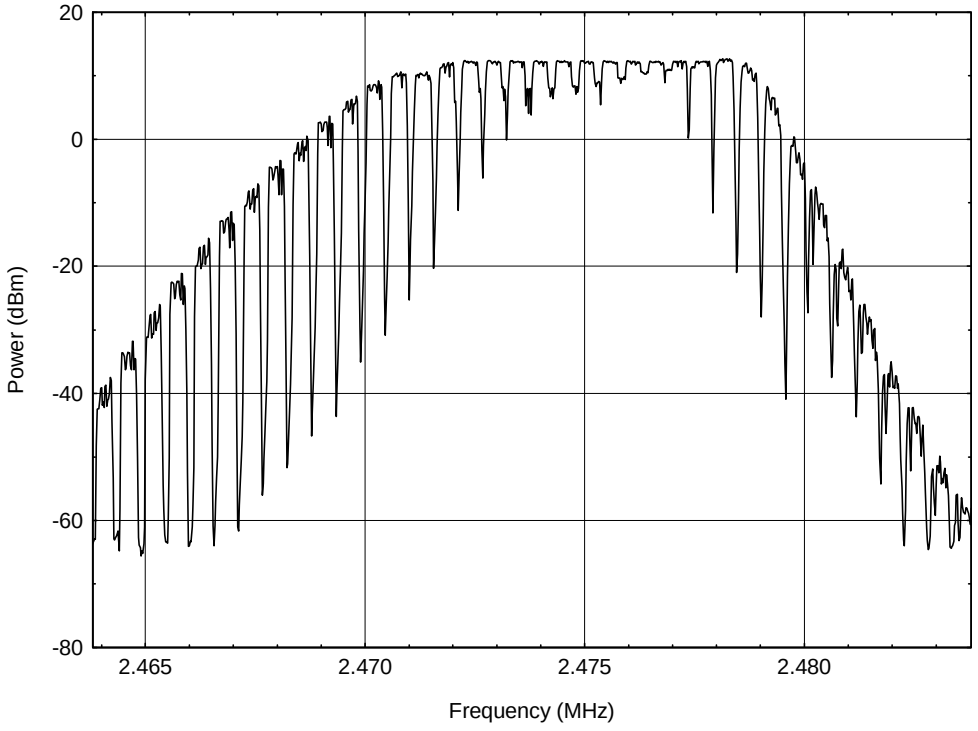

Figure A-28. Power measured with 6-cm loop located about 5-cm above center of RF coil (#4-99).

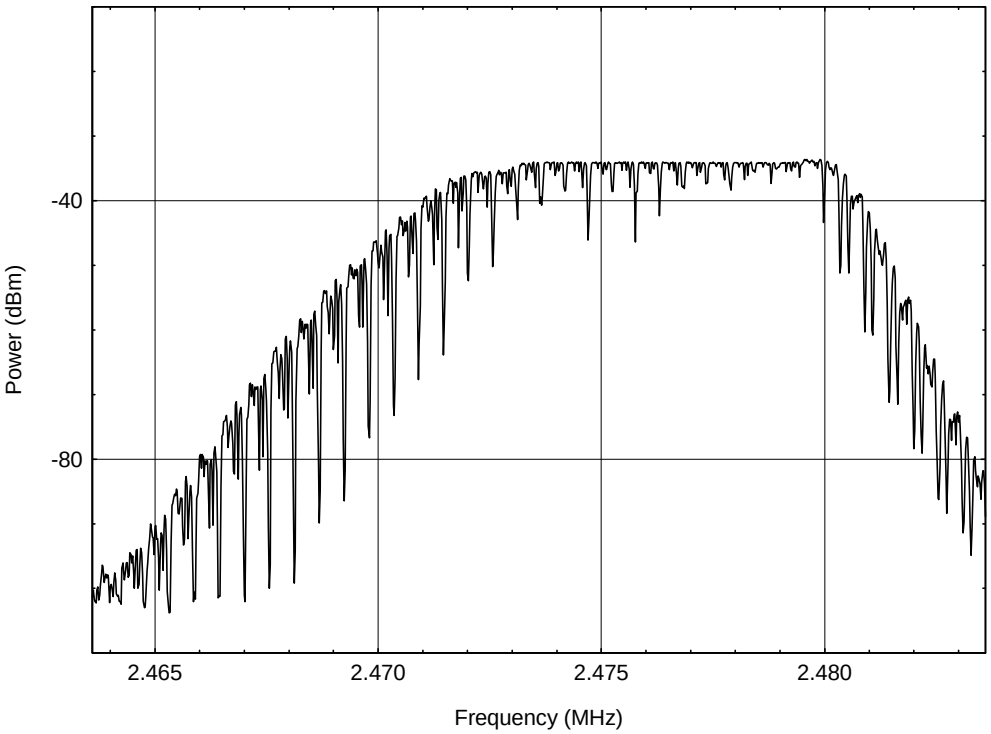

Figure A-29. Power measured with 12-in loop coxial with RF coil located 58-cm above the center of the coil (#5-8).

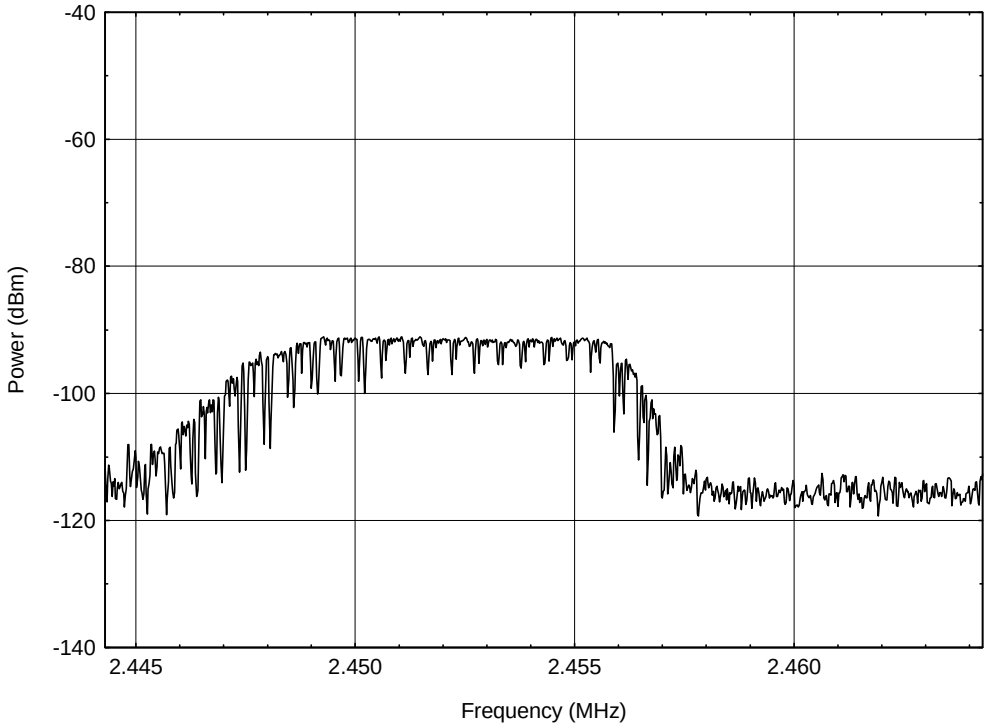

Figure A-30. E-field ball probe, distance to source R = 0.5m, spherical angle 2 = B/2 (#4-50).

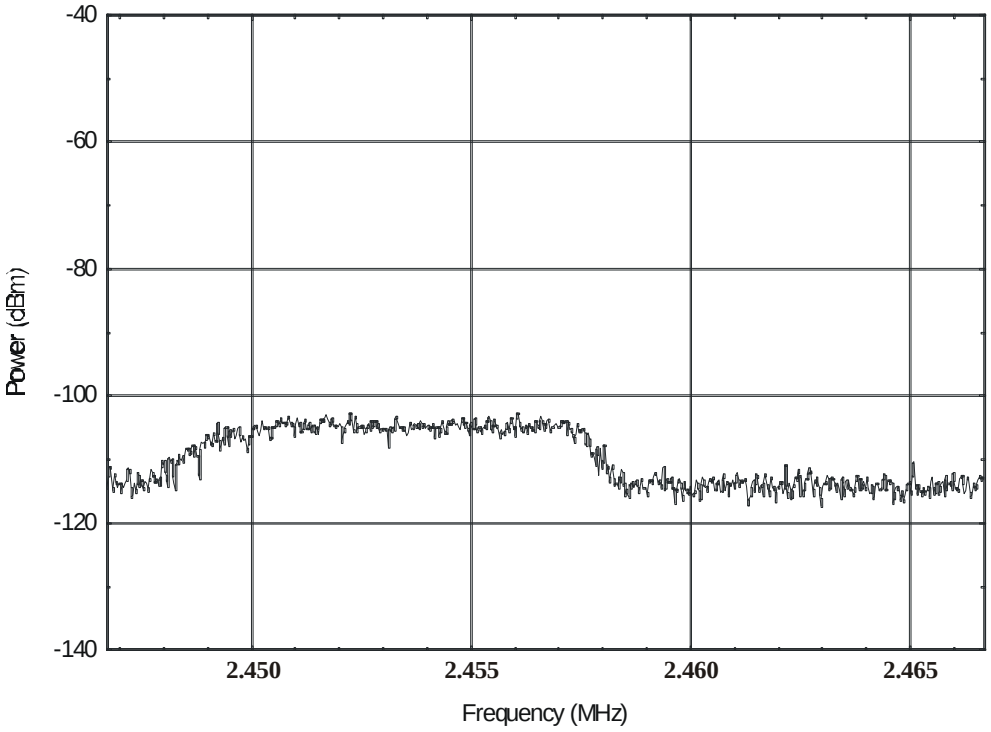

Figure A-31. E-field ball probe, distance to source R = 1.0 m, spherical angle 2 = B/2 (#4-47).

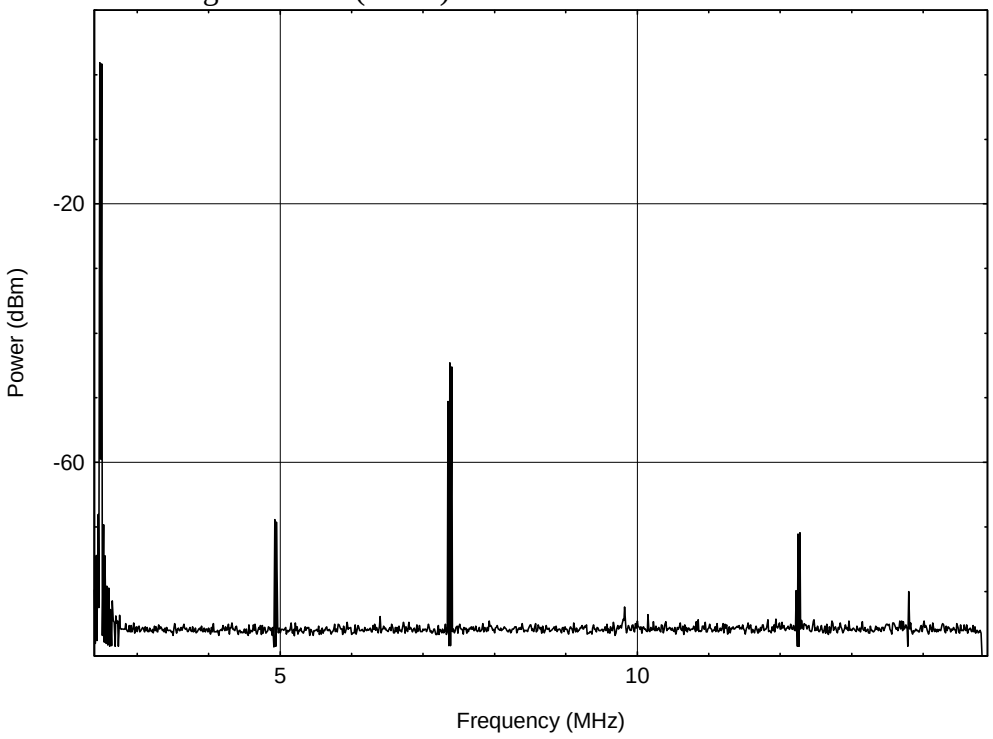

Figure A-32. Fundamental and harmonic frequencies measured with 12-in loop (#5-70).

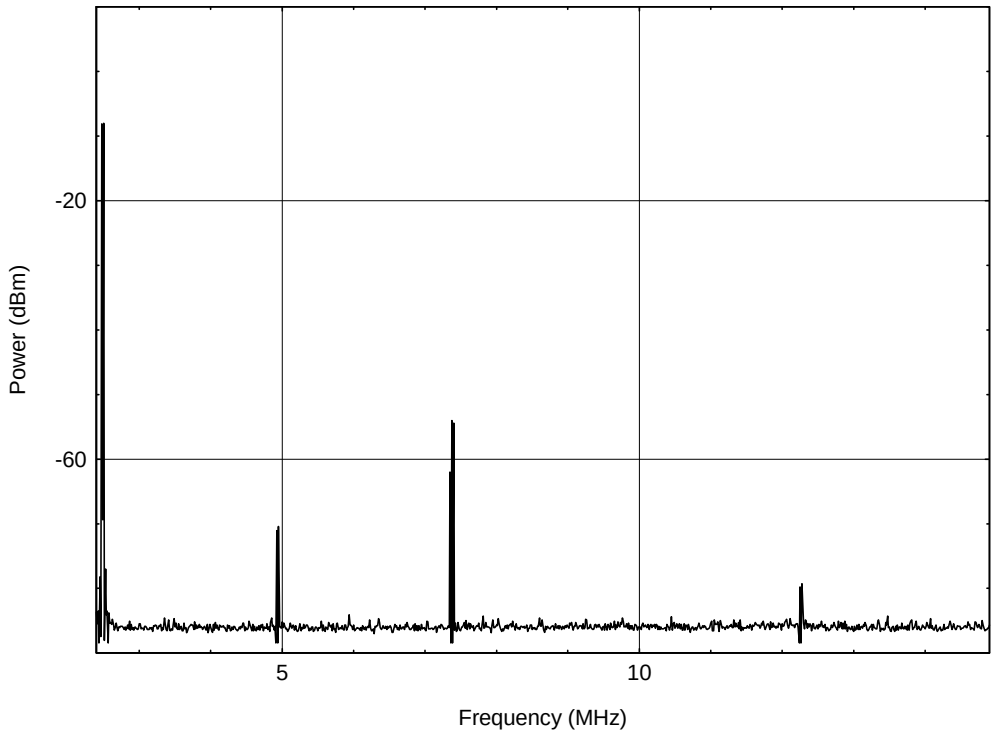

Figure A-33. Fundamental and harmonics with 10 dB pad measured with 12-in loop (#5-71).

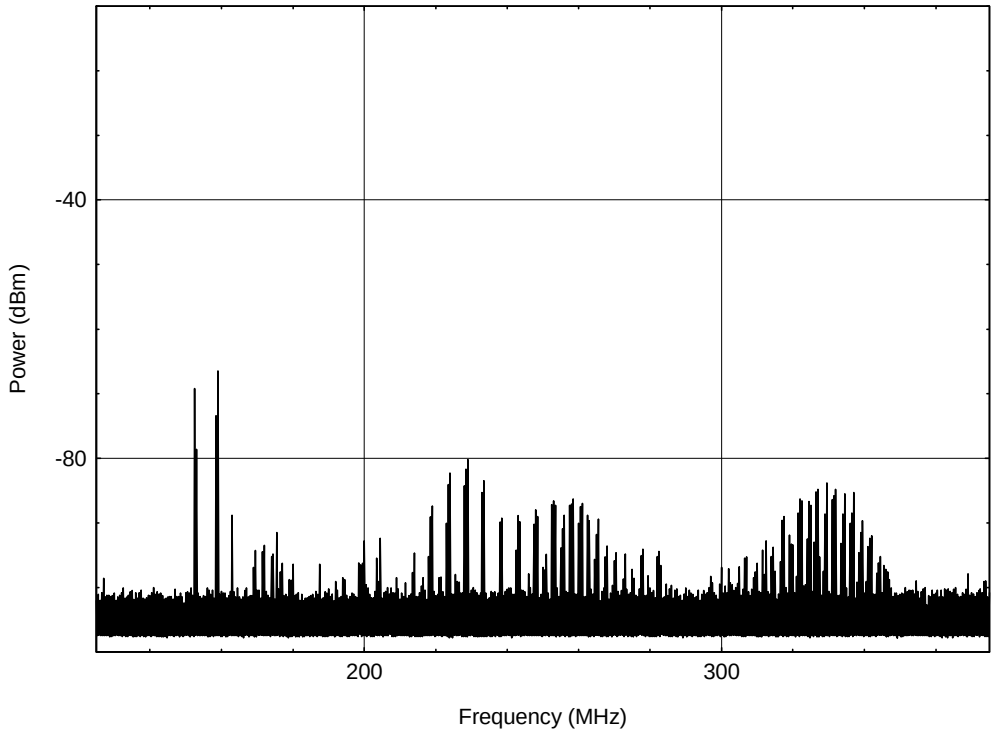

Figure A-34. E-field ball probe measurement located at the light (#5-28).

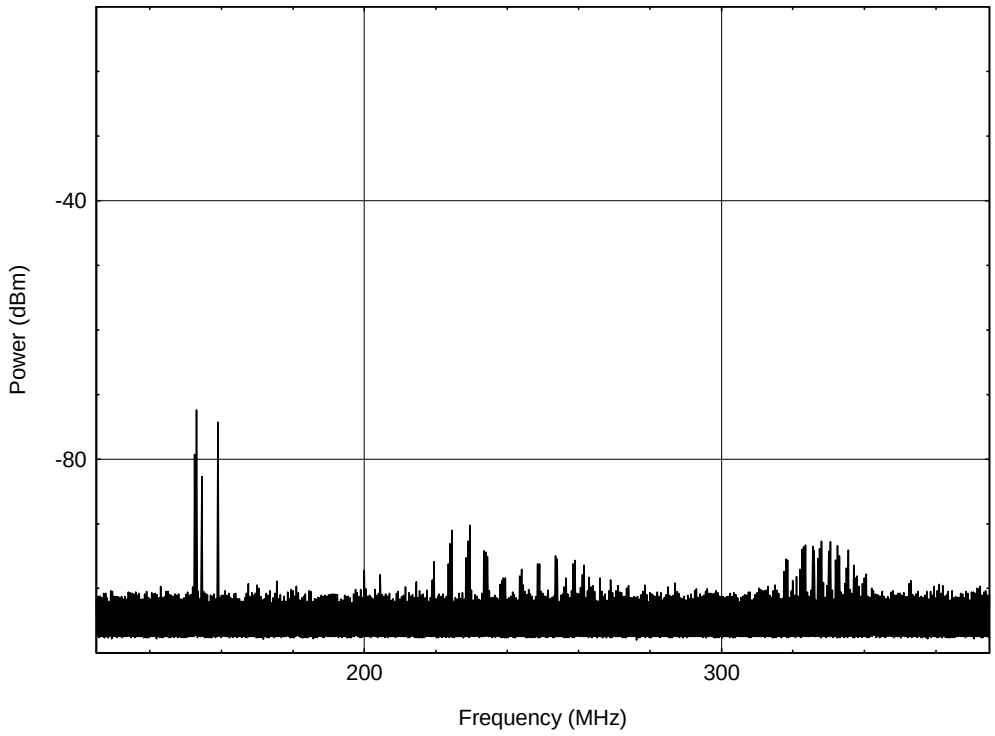

Figure A-35. E-field ball probe measurement (with 10 dB pad) located at the light (#5-30).

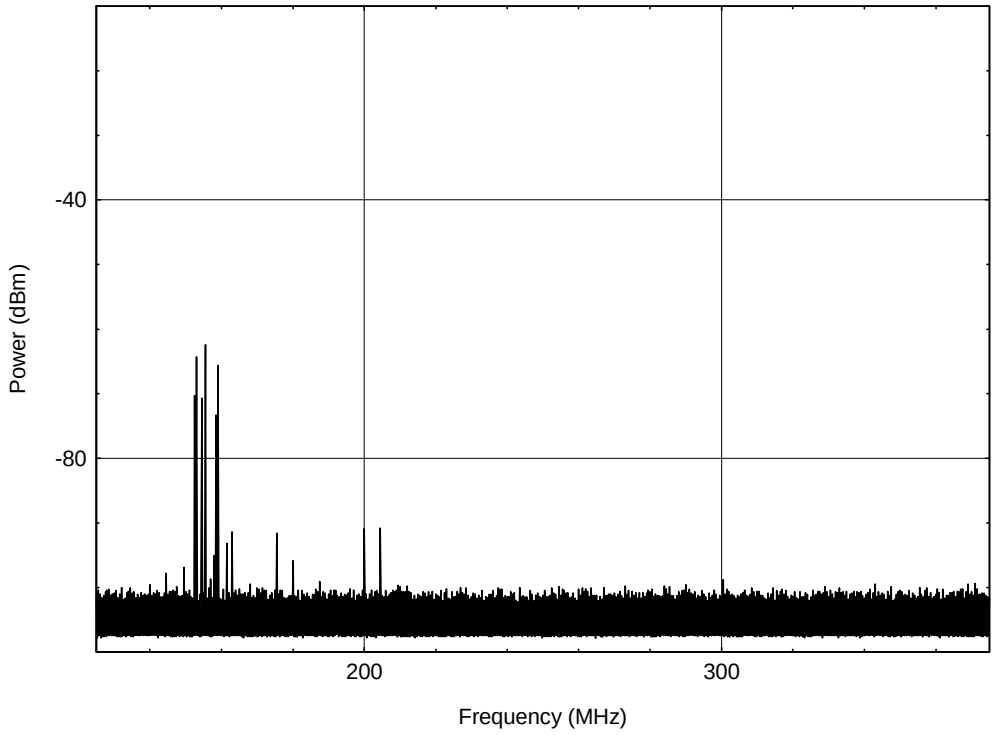

Figure A-36. Background e-field ball probe measurement (#5-29).

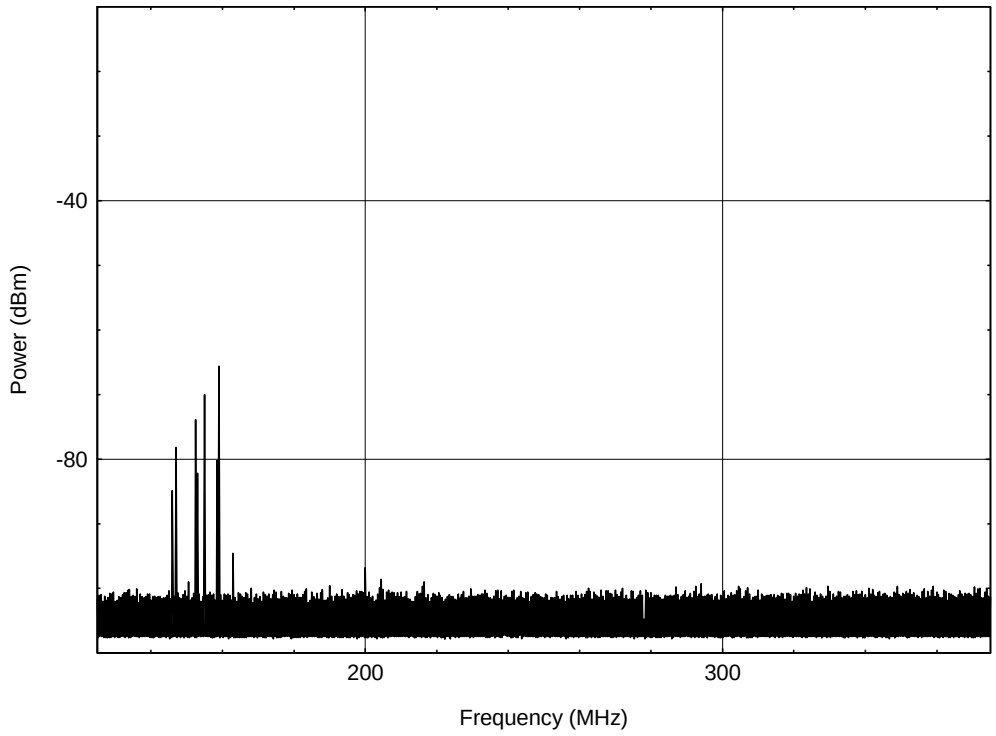

Figure A-37. E-field ball probe measurement, located 1 m from light bulb (#5-31).

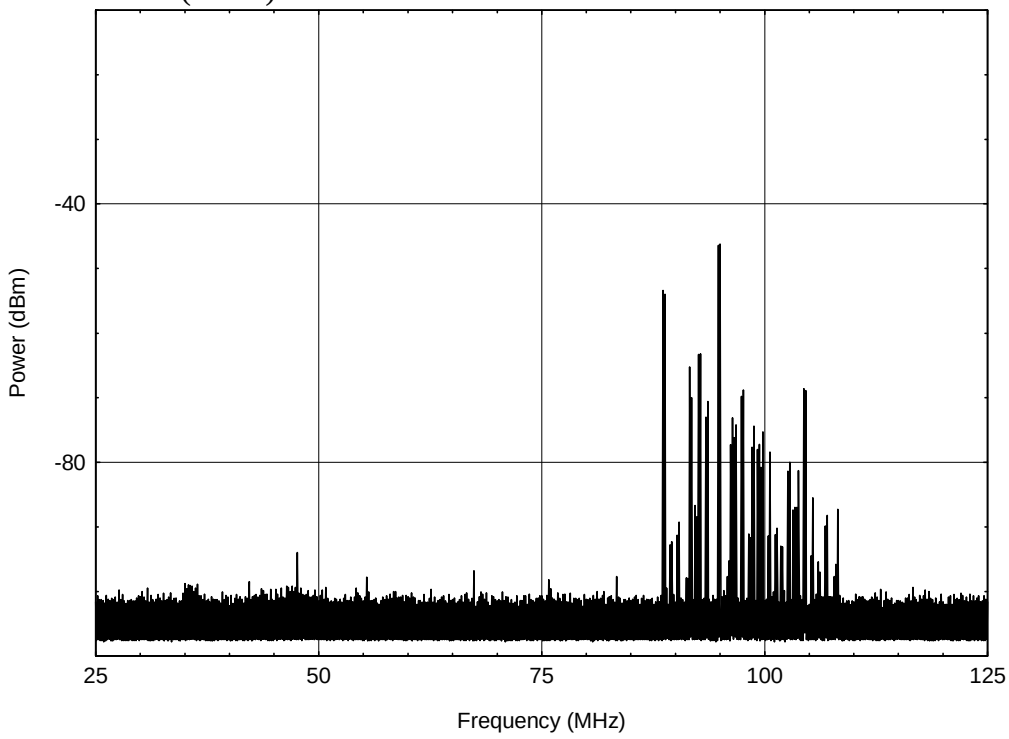

Figure A-38. Background e-field ball probe measurement, located 1 m from light bulb (#5-33).

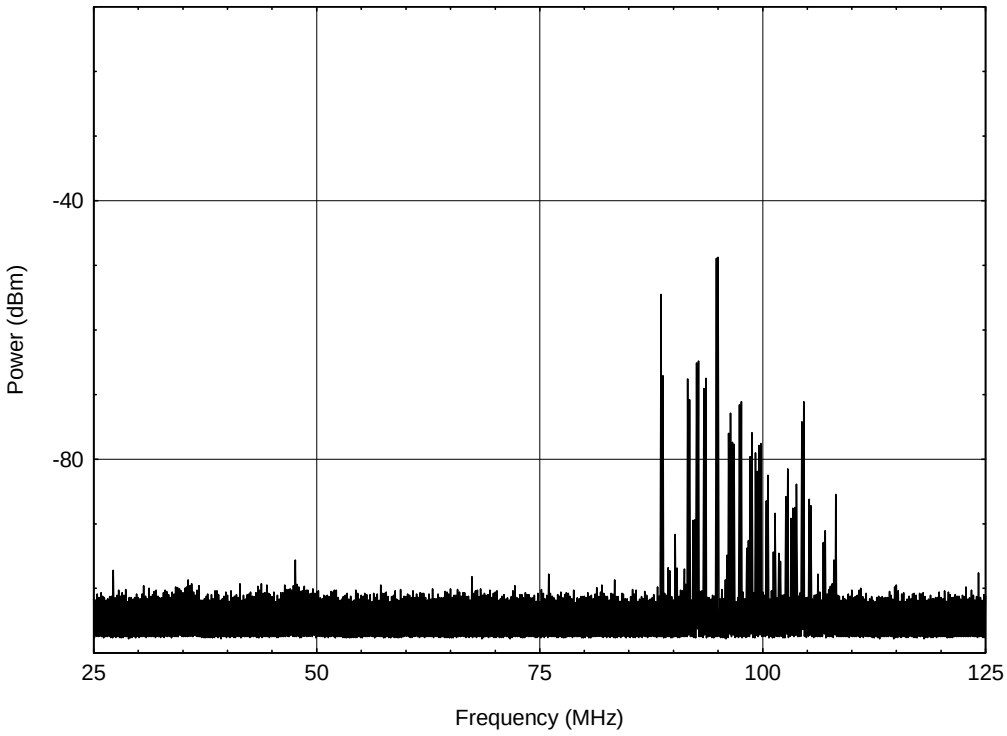

Figure A-39. E-field ball probe measurement, located 1 m from light bulb (#5-34).

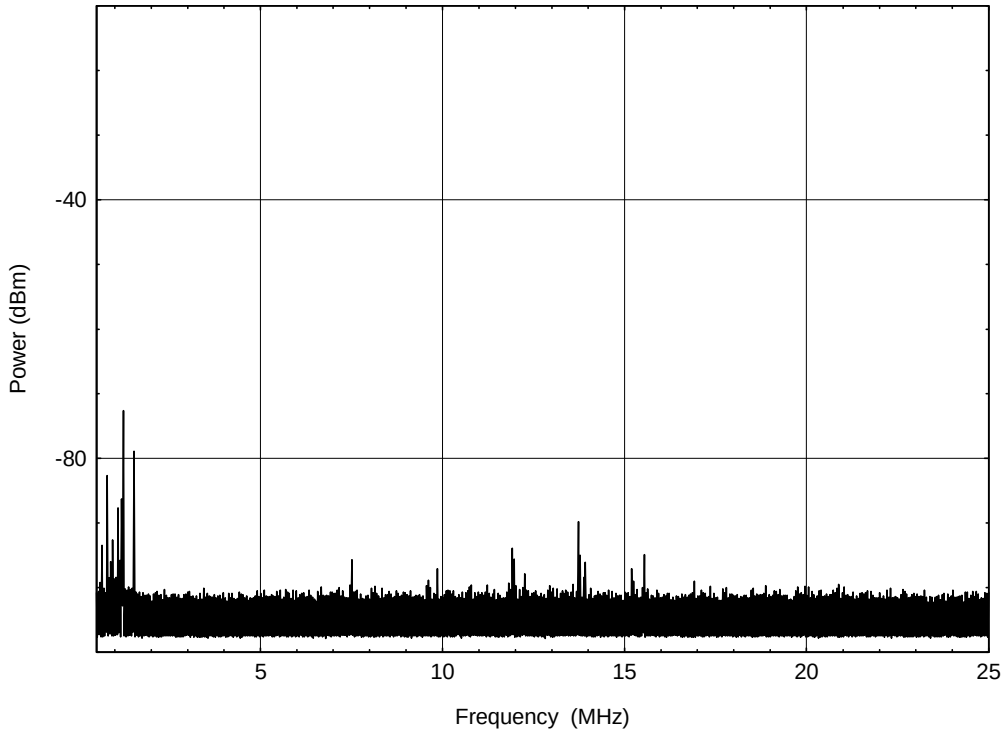

Figure A-40. Background e-field ball probe measurement (#5-35).

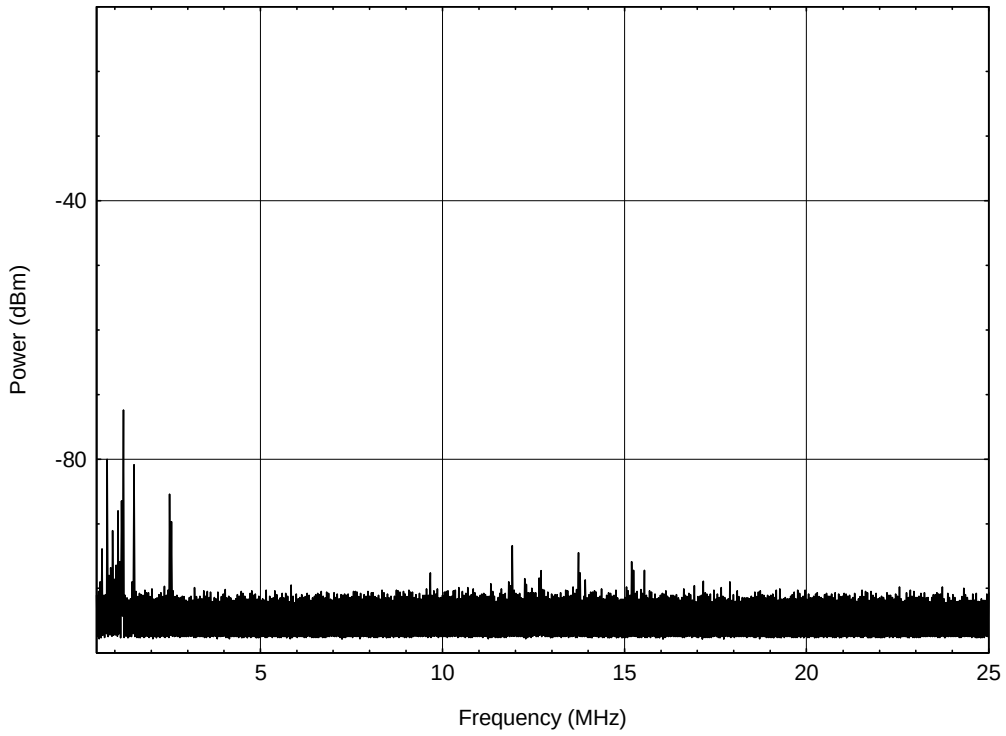

Figure A-41. E-field ball probe measurement, located 1 m from light bulb (#5-36).

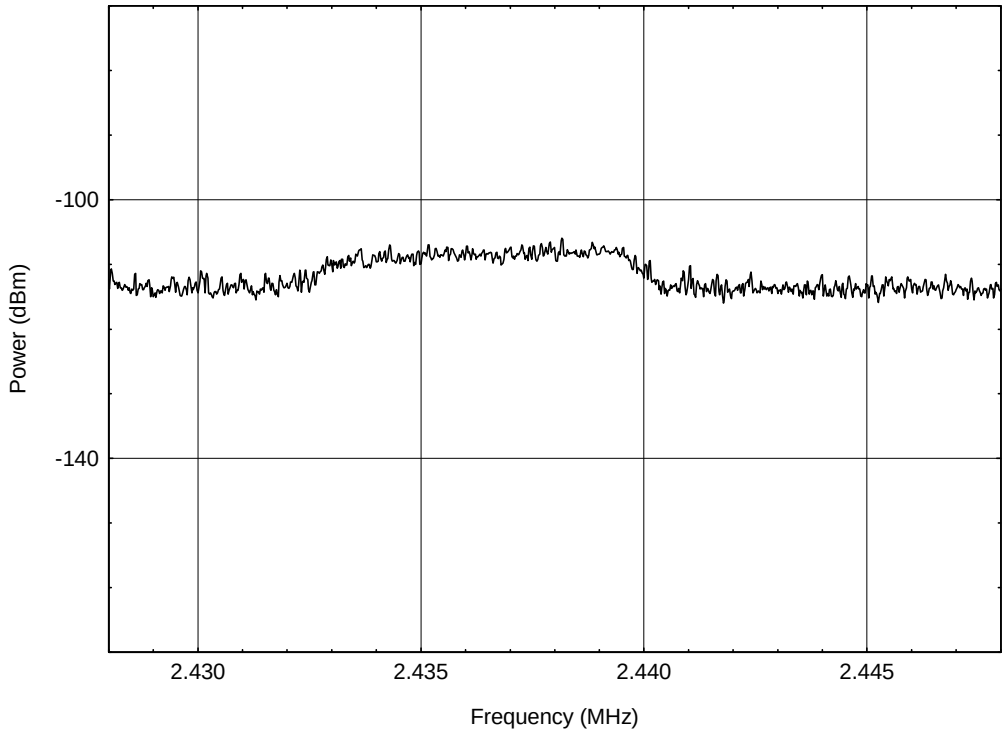

Figure A-42. Conducted current measurement (#5-73).

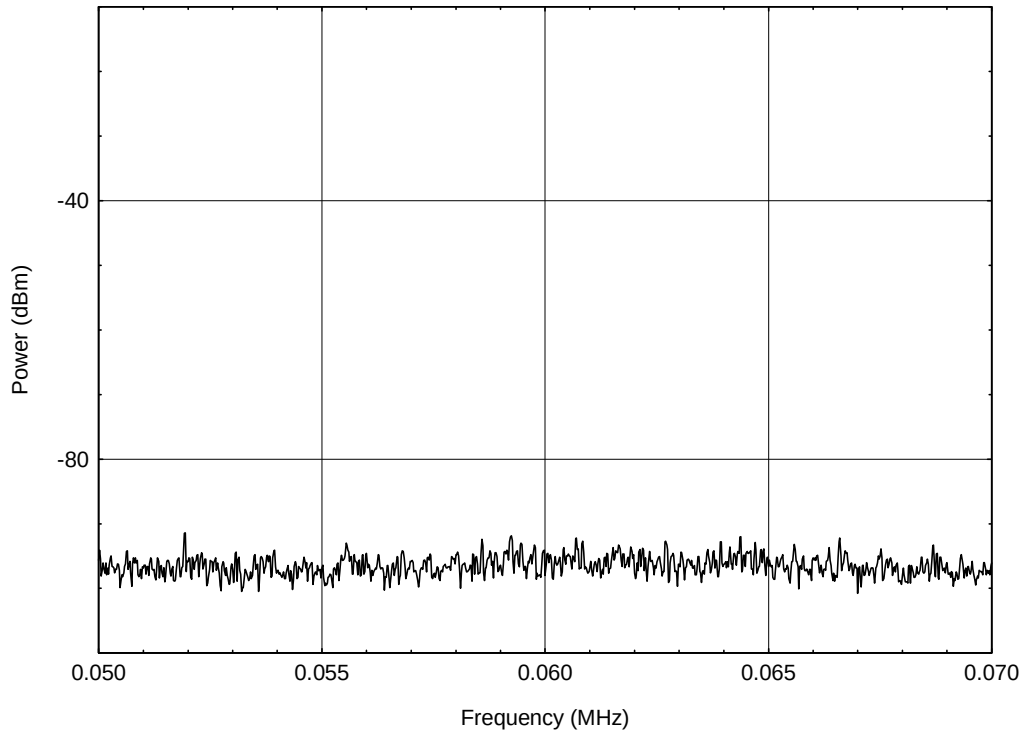

Figure A-43. Indoor measurement at 60 kHz using 12-in loop (#5-75).

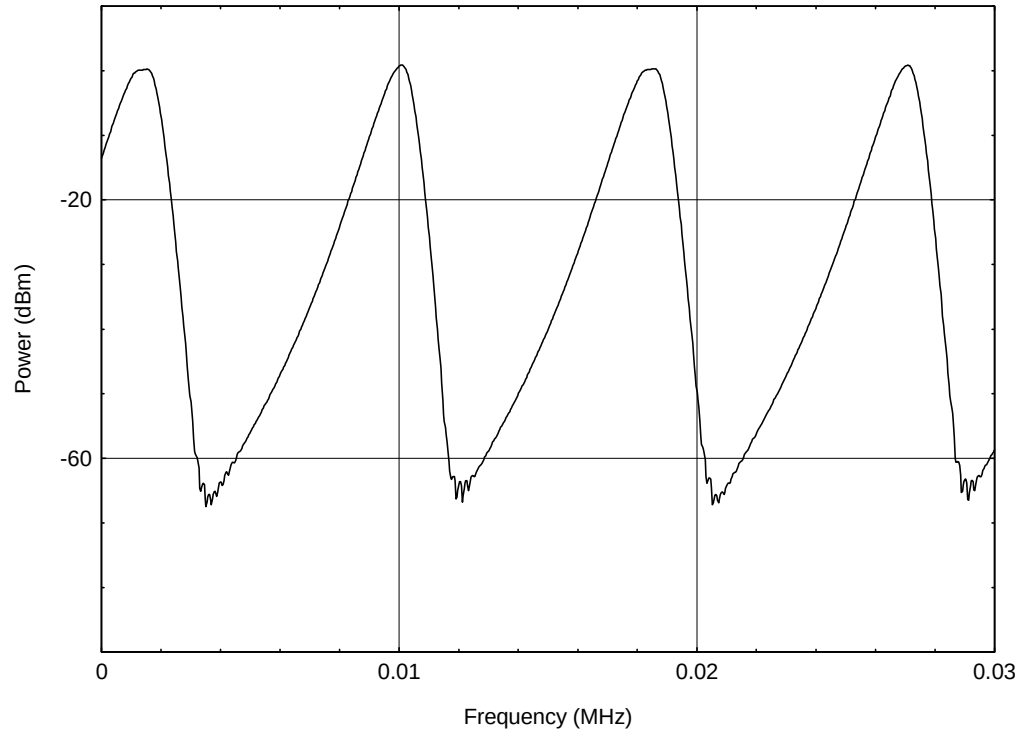

Figure A-44. Time domain envelope at 2.43272 MHz (#5-76).

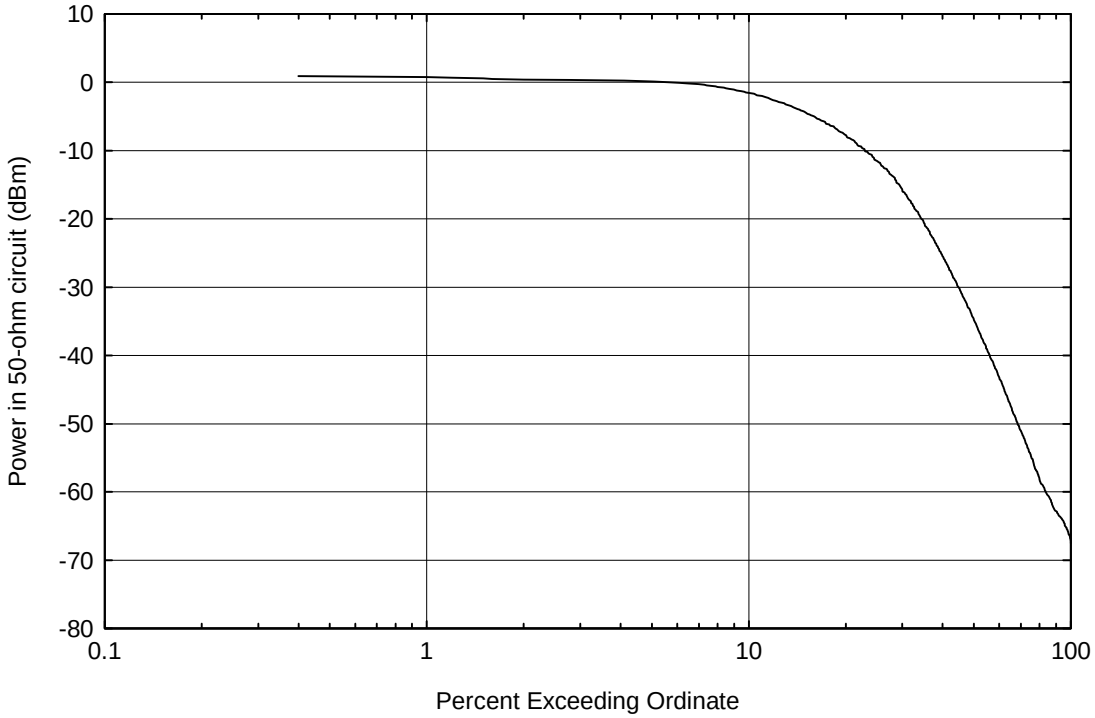

Figure A-45. APD for time domain envelope at 2.43272 MHz.

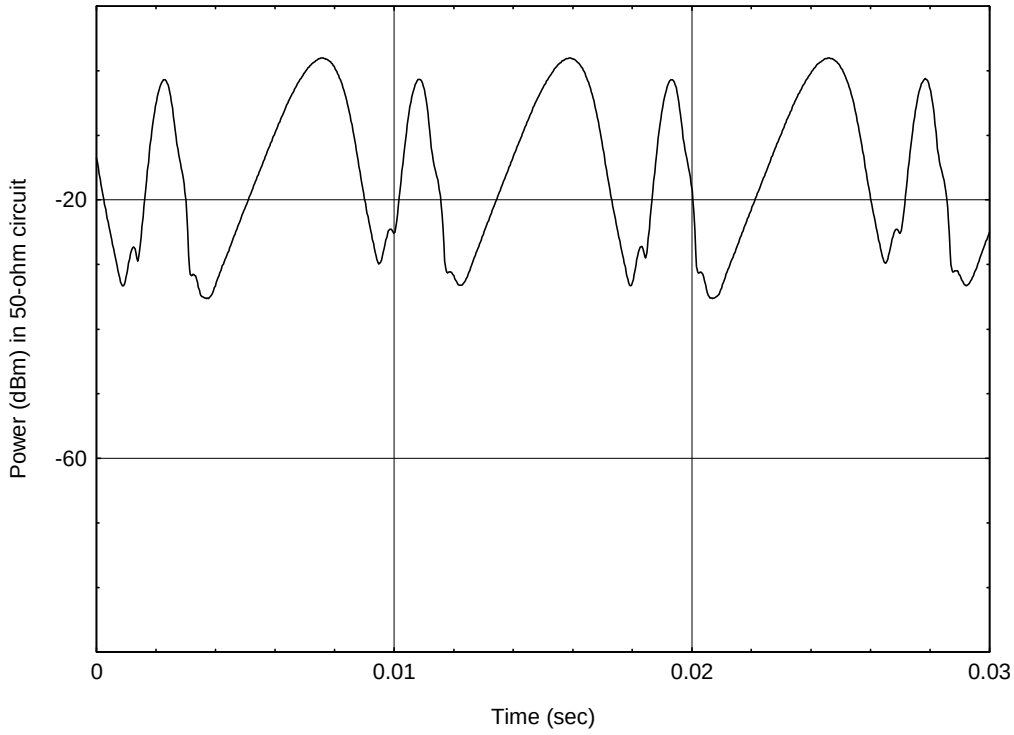

Figure A-46. Time domain envelope at 2.4544 MHz (#5-77).

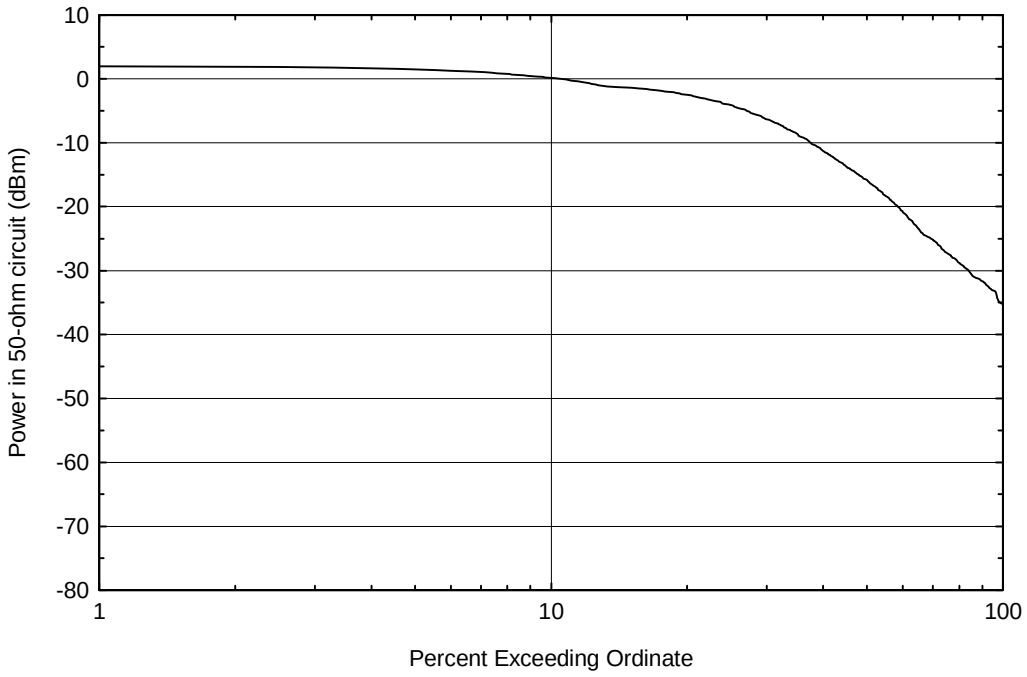

Figure A-47. APD for time domain envelope at 2.4544 MHz.

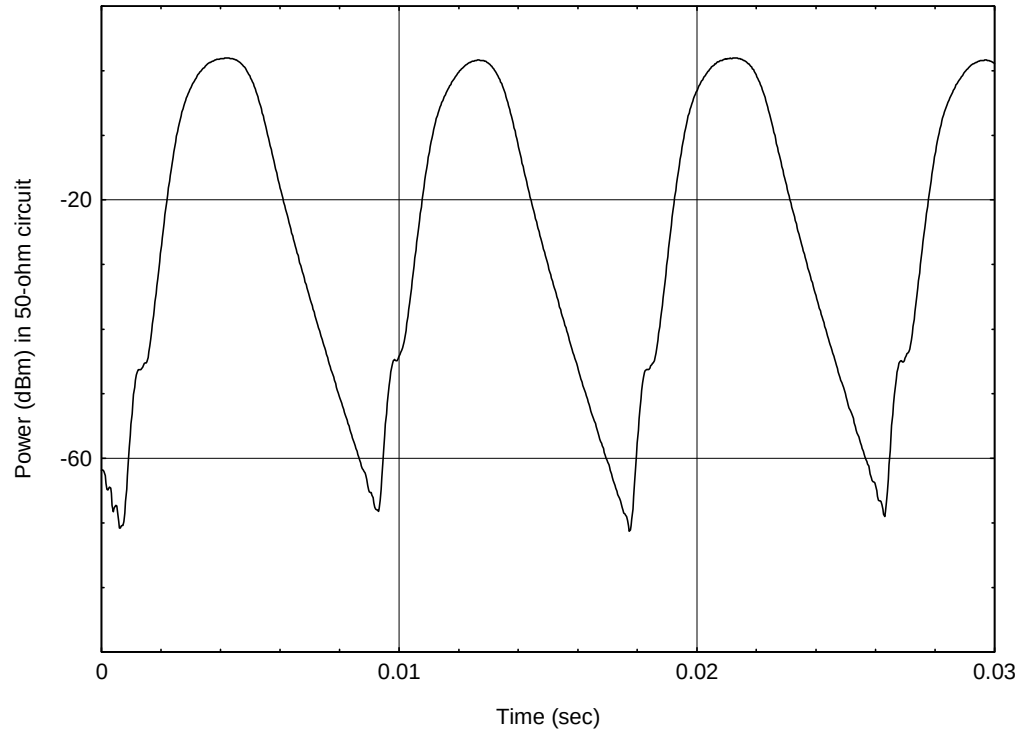

Figure A-48. Time domain envelope at 2.4804 MHz (#5-78).

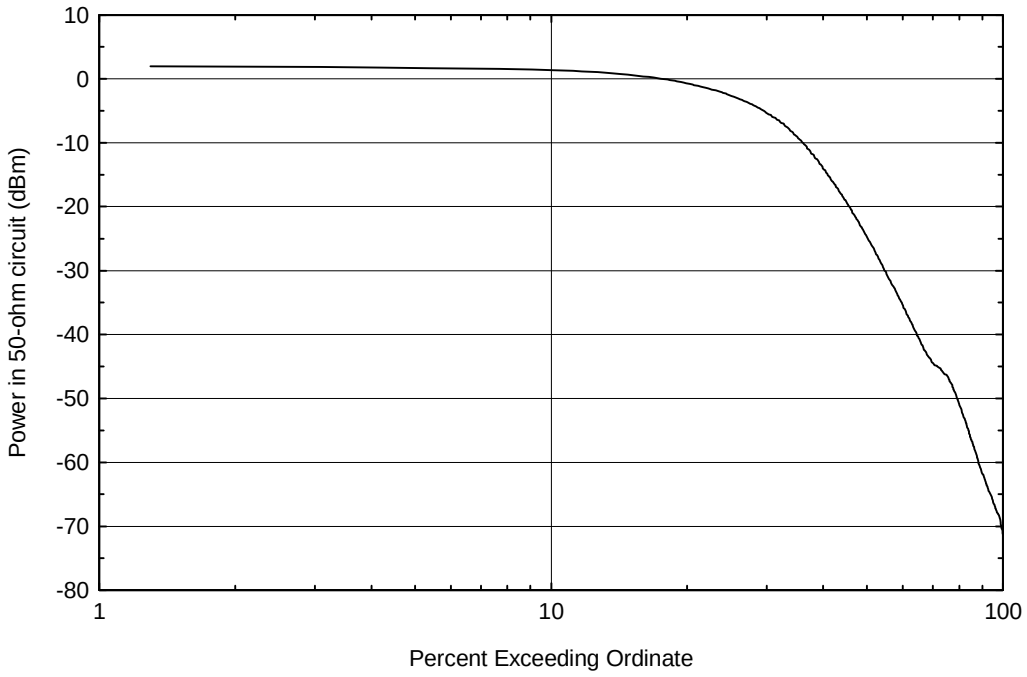

Figure A-49. APD for time domain envelope at 2.4804 MHz.

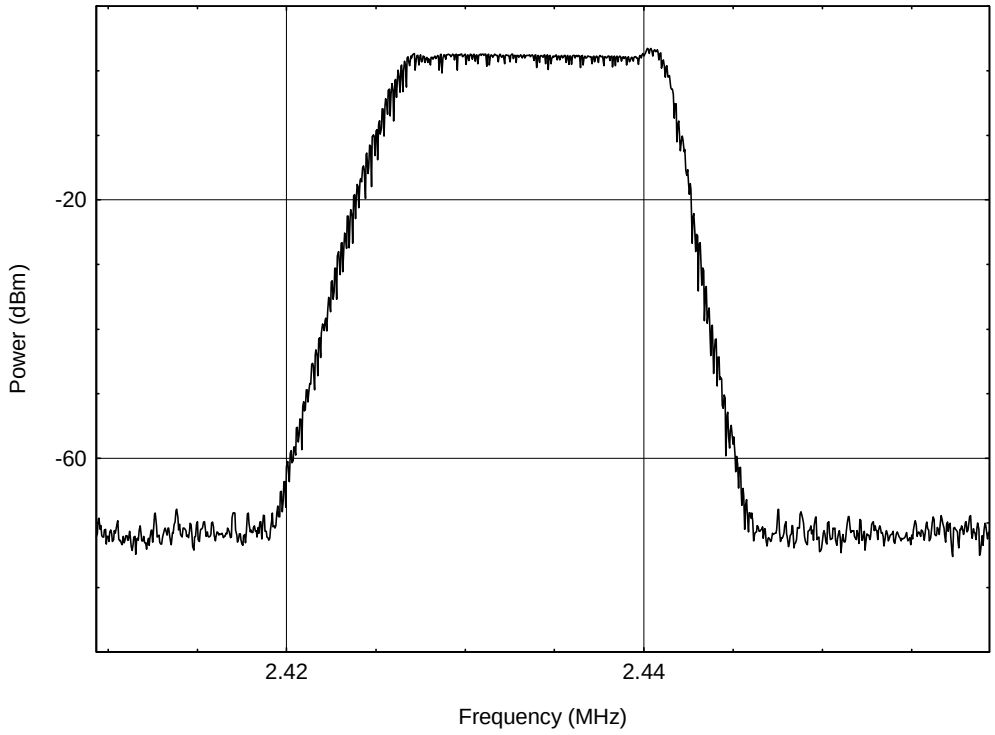

Figure A-50. Light bulb input voltage = 90V, indoor measurement using 12-in loop (#5-79).

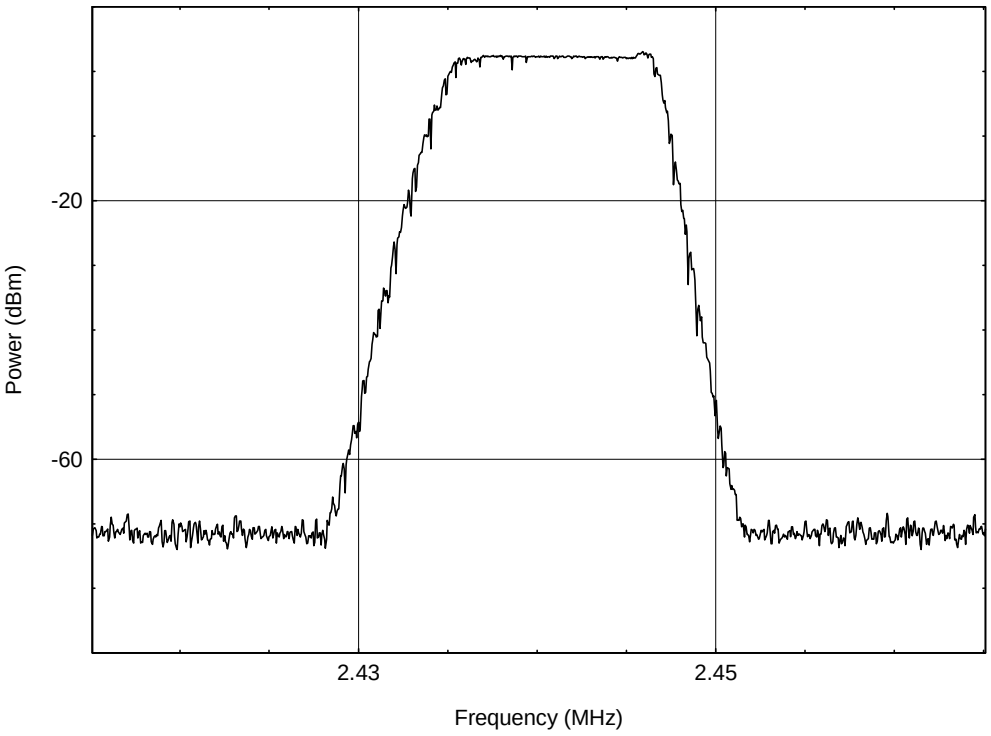

Figure A-51. Light bulb input voltage = 100V, indoor measurement using 12-in loop (#5-80).

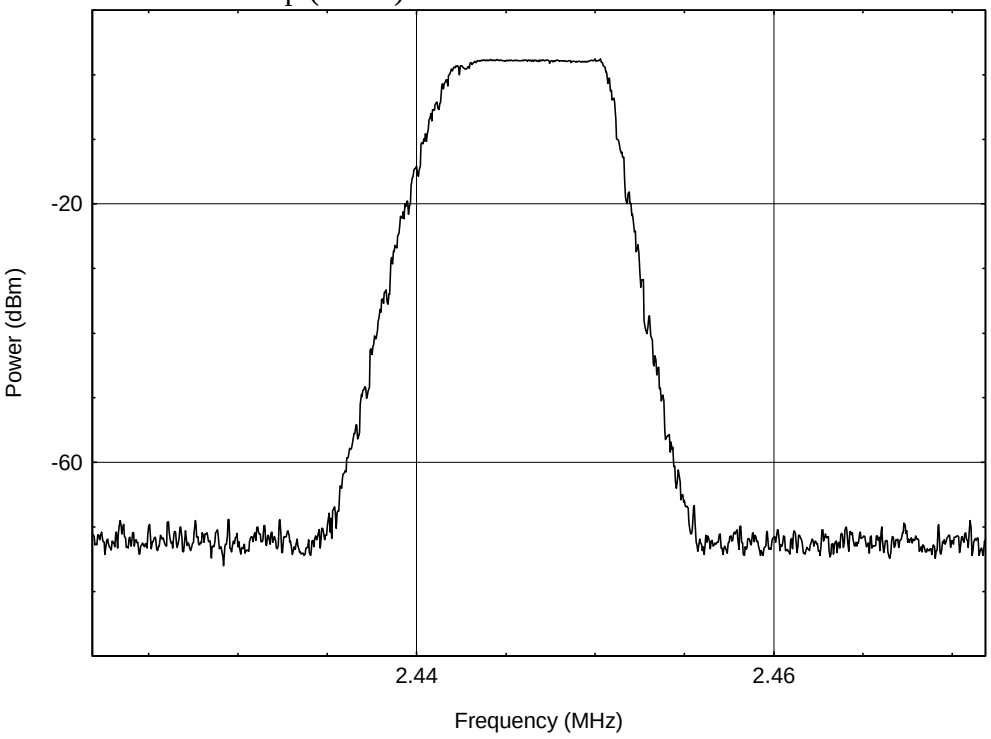

Figure A-52. Light bulb input voltage = 110V, indoor measurement using 12-in loop (#5-81).

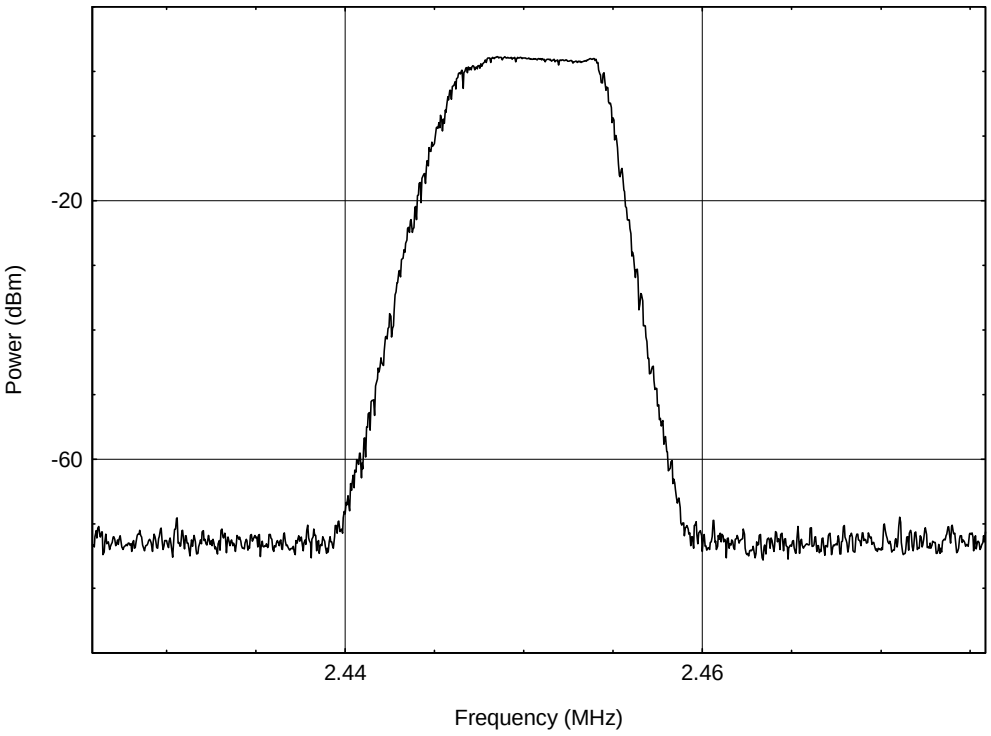

Figure A-53. Light bulb input voltage = 120V, indoor measurement using 12-in loop (#5-82).

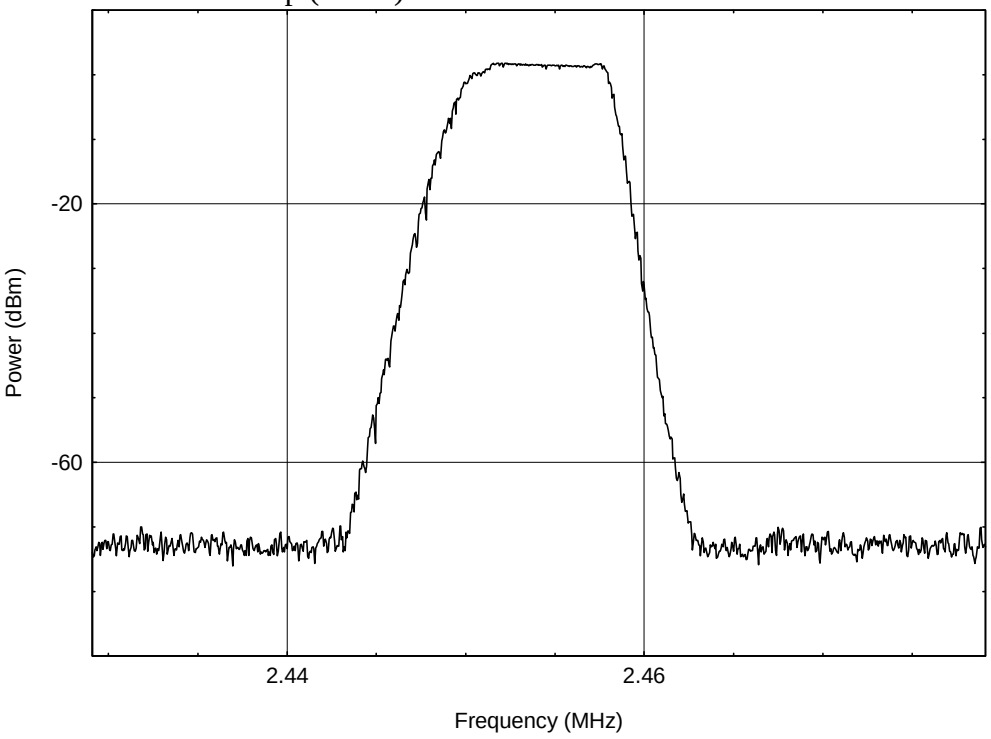

Figure A-54. Light bulb input voltage = 130V, indoor measurement using 12-in loop (#5-83).

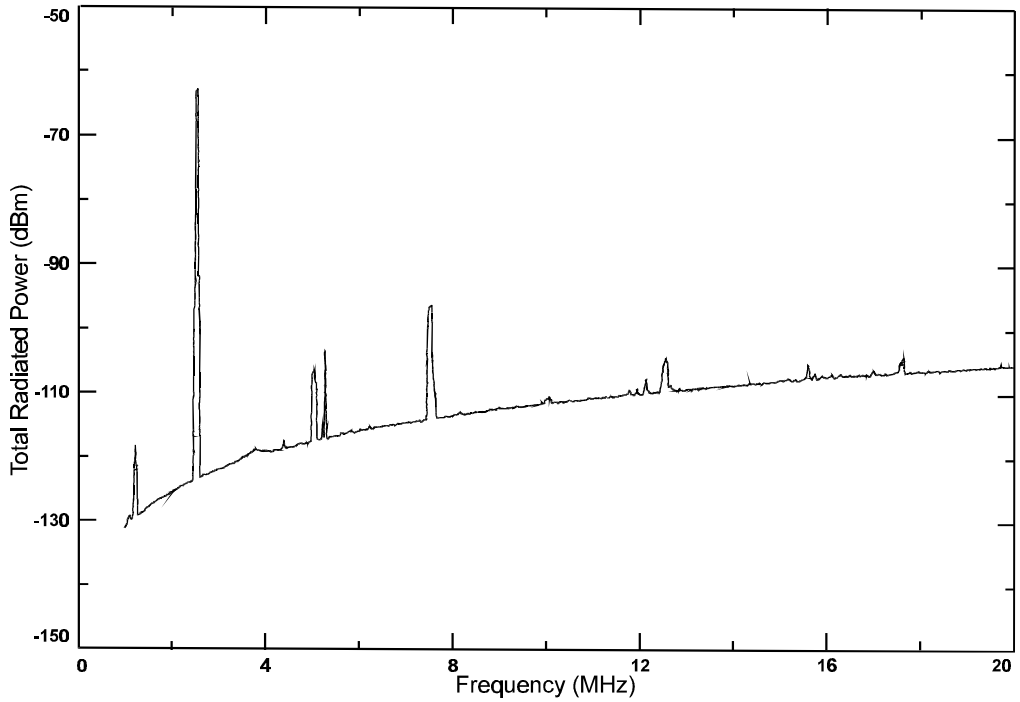

Figure A-55. Total radiated power as measured by the TEM cell (hybrid junction not rated below 2 MHz).

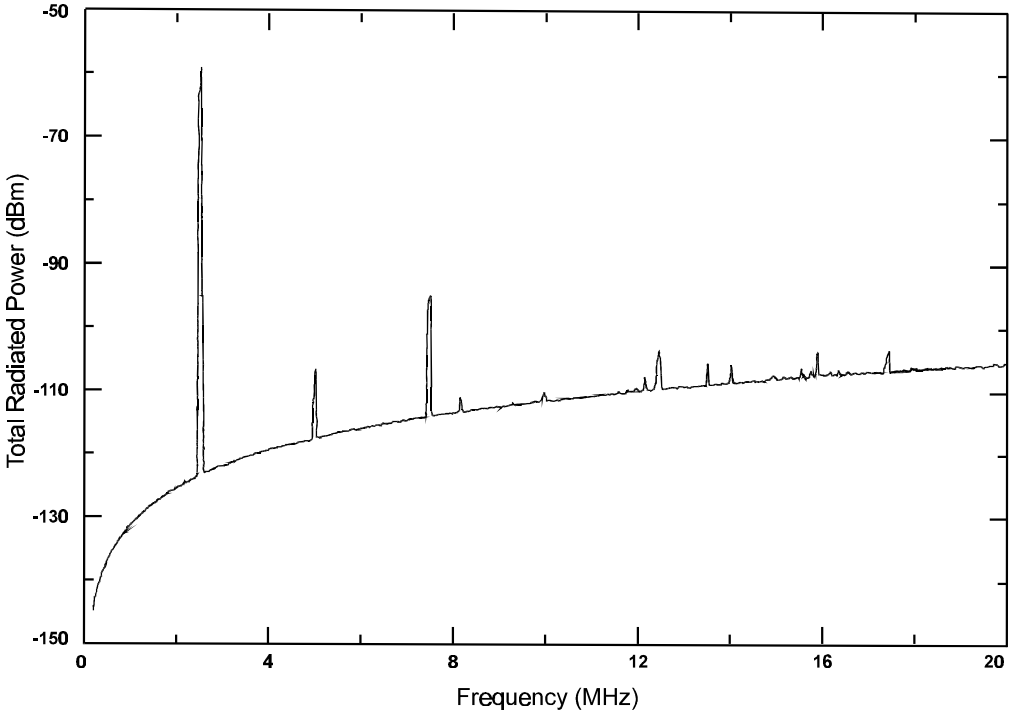

Figure A-56. Total radiated power as measured by the TEM cell (hybrid junction rated below 2 MHZ.